Alternative splicing dynamics during human cardiac development *in vivo* and *in vitro*

Beatriz Gomes-Silva [1,2*], Marta Furtado [2*], Marta Ribeiro [3], Sandra Martins [1,2], Maria Teresa Carvalho [1,2], Henrike Maatz [4], Michael Radke [4], Michael Gotthardt [4,5,6], Rosina Savisaar [1], Maria Carmo-Fonseca [1,2]

[1] Gulbenkian Institute for Molecular Medicine, Avenida Professor Egas Moniz, 1649-028 Lisboa, Portugal

[2] Faculdade de Medicina da Universidade de Lisboa, Avenida Professor Egas Moniz, 1649-028 Lisboa, Portugal

[3] Institute for Bioengineering and Biosciences and Department of Bioengineering, Instituto Superior Técnico, Universidade de Lisboa, Avenida Rovisco Pais, 1049-001 Lisboa, Portugal

[4] Max Delbrück Center for Molecular Medicine in the Helmholtz Association, Robert-Rössle-Strasse 10, 13125 Berlin, Germany

[5] Department of Cardiology, Charité-Universitätsmedizin Berlin, Hessische Strasse 3-4

10115 Berlin, Germany.

[6] DZHK (German Centre for Cardiovascular Research) partner site Berlin.

[*] These authors have contributed equally to the work.

Corresponding author:

M. Carmo-Fonseca, email: carmo.fonseca@gimm.pt

Key words: alternative splicing; cardiac myocytes; heart development; pluripotent stem cells

ABSTRACT

Cardiomyocytes differentiated *in vitro* from human induced pluripotent stem cells (iPSC-CMs) are increasingly used in studies of disease mechanisms, drug development, toxicity testing, and regenerative medicine. Alternative splicing (AS), a crucial mechanism for regulating gene expression during development, plays a pivotal role in cardiac differentiation and maturation. However, the extent to which iPSC-CMs recapitulate native cardiac splicing patterns remains poorly understood. Here, we provide a comprehensive temporal map of AS regulation during human cardiac development. In addition to the major splicing changes occurring perinatally, we identify finely tuned prenatal splicing transitions. While iPSC-CMs globally resemble the prenatal heart transcriptome, their splicing profiles are heterogeneous, with some splicing patterns mirroring the early embryonic tissue and others aligning with later stages. Moreover, we uncover altered splicing events in iPSC-CMs, including mis-splicing of splicing factors. In conclusion, we present a resource of AS dynamics throughout human cardiac development and a catalog of splicing markers to assess cardiomyocyte maturation *in vitro*. Our findings provide critical insights into the limitations of iPSC-CM models and their utility in cardiovascular research.

INTRODUCTION

Understanding human cardiac development is critical for advancing cardiovascular medicine and uncovering mechanisms underlying congenital and acquired heart diseases. Heart formation relies on the precise temporal control of gene expression programs, involving an evolutionarily conserved network of signaling pathways, transcription factors and epigenetic alterations [1–4]. These regulatory mechanisms govern the specification of cardiac cell fates and the differentiation and diversification of cardiac cell types throughout development [5].

A crucial mechanism that regulates gene expression during development is alternative splicing (AS), a process that expands transcript and protein diversity by generating multiple mRNA isoforms from a single gene [6,7]. Through AS of nascent transcripts (pre-mRNAs), individual genes produce a variety of mRNA species that may differ in stability, localization, or protein coding capacity [8–10]. Alternatively spliced protein isoforms may have related, distinct or even opposing functions [9,10]. Tissue-specific regulation of AS plays a crucial role in defining the identity and function of adult tissues, and its regulation is finely tuned during development [11–13].

AS plays a pivotal role in cardiac cell differentiation and maturation, with numerous splicing isoforms emerging at different developmental stages [14–16]. Recently, a cross-species comparison of splicing patterns across pre- and postnatal development of multiple organs revealed that splicing regulation is fundamental for heart development [17]. Despite these insights, a comprehensive characterization of AS during human cardiac development remains lacking. Furthermore, the physiological roles of developmentally regulated splicing isoforms are still poorly understood, limiting our ability to fully appreciate how splicing transitions contribute to heart formation and function.

Major advances in cardiac developmental biology have resulted from studies in murine models [18]. However, despite their utility, rodent heart architecture and cell function are very different from humans [19]. The discovery that differentiated adult human somatic cells can be reprogrammed into a pluripotent state [20] revolutionized the field, enabling the directed differentiation of pluripotent stem cells into well-defined cardiac lineages *in vitro*. Currently, human induced pluripotent stem cell-derived cardiomyocytes (iPSC-CMs) are widely used as an alternative to animal models for disease modeling, drug discovery, and toxicity screening [21].

Moreover, iPSC-CM transplantation is being explored as a potential strategy to repopulate damaged myocardial tissue and restore heart function [22].

Although iPSC-CMs are generally considered to resemble fetal cardiomyocytes [21], a systematic global comparison of splicing programs between iPSC-CMs and human hearts has yet to be performed. Such an analysis is crucial to understanding the extent to which iPSC-CMs recapitulate native cardiac splicing transitions and to identifying potential limitations in their maturation.

In this study, we conducted a comparative analysis of AS patterns in iPSC-CMs and human hearts across developmental stages, from early organogenesis to adulthood. Our findings provide a resource of developmentally regulated AS events, capturing splicing transitions that occur as the heart progresses from embryonic to postnatal life. While splicing profiles in iPSC-CMs globally resemble those of prenatal heart samples, we uncovered a subset of splicing events unique to iPSC-CMs, including mis-splicing of genes involved in RNA processing. Together, these findings provide a comprehensive characterization of AS dynamics during human heart development and establish a catalog of splicing events that can serve as benchmarks for assessing cardiomyocyte maturation *in vitro*.

RESULTS

Genome-wide comparison of splicing profiles in iPSC-CMs and developing hearts

To evaluate whether iPSC-CMs recapitulate the splicing patterns of the heart and determine the developmental stage they most closely resemble, we directed the differentiation of three independent iPSC lines (referred to as D, G, and T, **Figure 1A**) into cardiomyocytes (see **Methods**). The majority of differentiated iPSC-CMs exhibited cardiomyocyte-like morphology, including an elongated shape and well-defined sarcomere structures (**Figure 1B, C**).

To assess which cell types were present in monolayer cultures of iPSC-CMs at day 30 of differentiation, we conducted single-cell RNA sequencing (sequencing metrics in **Table S1**). The results revealed that 84–88% of cells expressed gene signatures characteristic of cardiomyocytes (**Figure 1D**, **Figure S1A**), including the expression of sarcomeric and mitochondrial genes

(**Figure S1B, C**). In contrast, ~12-16% of cells were enriched in *TNNT1*, the predominant troponin isoform during early cardiac development, as opposed to *TNNT2*, which is characteristic of fully mature cardiomyocytes (**Figure S1B**). Label transfer annotation using the Cui et al. single-cell atlas [23] indicated that these cells resembled the gene expression profiles of 5-week human embryonic hearts (**Figure S1D**). These cells also displayed expression of epicardial markers, including *WT1*, *UPK3B* and *ALDH1A2* (**Figure S1B**) [23,24]. The epicardial-like cells were enriched in extracellular matrix-related pathways, whereas the cardiomyocyte population showed enrichment in cardiac development pathways (**Figure S1E**). This observation aligns with studies reporting the bifurcation of cardiac progenitors into myocardial and epicardial lineages during both iPSC differentiation [25] and mouse cardiac development [26].

Next, we conducted bulk RNA-sequencing (RNA-seq) of polyadenylated RNA isolated from the three iPSC-CM lines at day 30 of differentiation (sequencing metrics in **Table S1**). To assess the reproducibility of our differentiation protocol, we performed pairwise comparisons of gene expression profiles among the three samples (**Figure S1F**). Pearson correlation coefficients were higher than 0.98, similarly to the correlation observed between two heart tissues of the same developmental age (**Figure S1F**). Additionally, we noted a substantial overlap in transcribed genes across all three lines (**Figure S1G**).

To understand how the transcriptomes of iPSC-CMs compare with gene expression profiles during heart development, the three data sets from iPSC-CM cultures were grouped as biological replicates and compared with publicly available bulk RNA-seq datasets from human heart samples, spanning from early organogenesis to adulthood [27]. This dataset comprises 38 prenatal samples collected between 4 and 19 weeks post-conception, and 12 postnatal samples collected from newborns, infants, young children, and adults (**Figure 1E**). To explore the primary sources of variation in gene expression profiles of iPSC-CMs and human hearts at distinct developmental stages, we performed principal component analysis (PCA). This analysis revealed that the first principal component (PC1), accounting for 51% of the variance, effectively distinguishes prenatal heart samples from postnatal samples, capturing progressive transcriptional changes throughout development (**Figure 1F**). Along PC1, the iPSC-CMs clustered most closely with 8–10 week prenatal heart samples (**Figure 1F**). Hierarchical clustering revealed that the iPSC-CMs cluster closer to the prenatal heart than to the postnatal heart samples, and bootstrapping

confirmed the reliability of the clustering, attributing 100% confidence (approximately unbiased p-value * 100) to the node that clusters the iPSC-CMs with the prenatal hearts (**Figure S1H**).

To identify and quantify alternative splicing (AS), we used rMATS, MAJIQ, and vast-tools, focusing on the most common patterns of AS events (i.e., exon skipping, alternative 3' and 5' splice sites, and intron retention). Pairwise comparisons of the inclusion levels of all AS events detected in the three iPSC-CM cultures revealed Spearman correlation coefficients of ~0.93, higher than that observed between embryonic hearts of the same developmental age (**Figure S1I**). The three iPSC-CM datasets were grouped and compared with heart datasets. While PCA of splicing data was noisier than that of gene expression, considering that developmental time is captured by the combination of the two principal components, iPSC-CMs consistently clustered closer to the prenatal samples, across all three tools (**Figure 1G**, **Figure S1J, K**). Given the distinct cell type composition of iPSC-CMs and heart tissues, differences in splicing patterns could be influenced by sample heterogeneity. To account for this, we used CIBERSORTx to deconvolute the bulk expression data into distinct cell types. We found that, unlike iPSC-CMs, which were highly enriched in cardiomyocytes, prenatal heart samples contained a more diverse mix of cell types and a relatively lower proportion of cardiomyocytes (**Figure 1H**). Importantly, the cardiomyocyte content of iPSC-CMs was more similar to postnatal than to prenatal samples, suggesting that their clustering with the latter is unlikely to be driven by patterns of cell type composition. (**Figure S1M**).

Pairwise differential splicing analysis, focusing on identifying events with a deltaPSI (difference in Percent Spliced In) higher than 20%, revealed 415 differentially spliced events between prenatal and postnatal heart samples (**Figure 1I, Table S2**). When comparing iPSC-CMs and heart samples, we found 948 splicing events differing between *in vitro* cultures and prenatal samples, and 877 events dissimilar between *in vitro* differentiated cardiomyocytes and postnatal heart samples (**Figure 1I, Table S3**). Alternative ''cassette'' exon and intron retention were the most frequent types of alternative splicing identified (**Figure 1I**).

Hierarchical clustering of differentially spliced events revealed distinct patterns of exon usage and intron retention across developmental stages. Exons predominantly skipped in prenatal hearts were grouped in cluster 1, while those primarily skipped in postnatal hearts were grouped

in cluster 4 (**Figure 1J**). Additionally, a skew toward increased intron retention was observed in prenatal hearts (**Figure S1N** – cluster 3). This analysis further revealed exon skipping events that uniquely distinguish iPSC-CMs from both prenatal and postnatal hearts (**Figure 1J** – clusters 2 and 3), as well as intron retention events specific to iPSC-CMs (**Figure S1N** - cluster 2).

In conclusion, our genome-wide comparison of RNA-seq datasets from iPSC-CMs and developing human hearts demonstrates that iPSC-CMs exhibit a transcriptional and splicing landscape that more closely resembles that of early prenatal heart samples.

Pre- to postnatal splicing transitions in the heart

Among the 415 events that are differentially spliced between prenatal and postnatal heart samples (**Table S2**), we found several alternative ‘‘cassette’’ exons previously described as developmentally regulated during cardiac maturation. For example, EH-myomesin is an embryonic-specific isoform of *MYOM1* characterized by the inclusion of exon 18. This exon encodes a protein domain that promotes elasticity and modulates viscoelastic proprieties of the sarcomere [28]. We observed a progressive decrease of *MYOM1* exon 18 inclusion during development (**Figure 2A**). After birth, the majority of isoforms exclude exon 18, and in adult hearts this exon is totally absent. In iPSC-CMs, *MYOM1* exon 18 is almost entirely included (median > 94%), similarly to 4-7 weeks prenatal hearts (**Figure 2A**). Another example is *MBNL1* exon 5, which has been described as developmentally regulated in mice and chicken [29]. In human hearts, we found lower levels of exon 5 inclusion in postnatal hearts compared to prenatal hearts, and in iPSC-CMs the inclusion level was similar to prenatal hearts (**Figure 2B**). Using vertical agarose gel electrophoresis to resolve titin protein isoforms [30], we found that iPSC-CMs express higher molecular weight fetal N2BA splicing isoforms but not adult N2BA or N2B (**Figure S2A**), which is the dominant titin isoform in the adult heart [31].

Our analysis identified a substantial number of novel splicing events that differ between pre- and post-natal hearts (**Table S4**). To investigate the potential functional significance of these events, we used *VastDB* and *NEASE* to predict their effects on protein function and interactions. A striking enrichment of splicing events predicted to impact proteins associated with the

extracellular matrix (ECM) was observed (**Figure 2C**). Among affected ECM genes, we observed alternative splicing of fibronectin (*FN1*) exons 25 (**Figure 2D**) and 33 (**Figure S2B**), corresponding to the EDB and EDA isoforms [32]. We also observed AS changes in Kindlin-2 (*FERMT2*), a regulator of integrin-mediated cell adhesion and ECM remodeling [33]. In the adult heart, we found increased inclusion of exon 11 (**Figure 2E**), which encodes a domain involved in various protein interactions. During heart development, we further detected increased inclusion of Fibulin-2 (*FBLN2*) exon 9 (**Figure S2C**), which encodes a calcium-binding EGF domain [34].

Novel AS changes predicted to impact muscle contraction include *TNNT2* exon 13 (**Figure S2D**), *TPM3* exon 5 (**Figure S2E**), *ACTN4* exon 8 (**Figure S2F**), and *MYL6* exon 6 (**Figure S2G**). In all cases, iPSC-CMs displayed splicing patterns resembling those of prenatal hearts.

Furthermore, we detected splicing changes in the transcription factor *MEF2D*, with increased inclusion of exon 8, which encodes a domain essential for transcriptional activation [35], occurring after birth (**Figure S2H**). Increased inclusion of *TCF3* exon 18, which encodes the DNA-binding domain of this transcription factor [36], was also observed after birth (**Figure S2I**). Increased inclusion of *MLF1* exon 3, which disrupts a domain required for cell cycle control [37] was further detected in postnatal hearts (**Figure S2J**).

Additionally, we identified AS events in metabolism-related genes. We observed a progressive decrease in inclusion of *IMMT* exon 6 during development, particularly after birth (**Figure 2F**). Strikingly, in this case, iPSC-CMs more closely match the inclusion levels of postnatal hearts (**Figure 2F**). *IMMT* encodes the mitochondrial protein mitofilin [38], and its exon 6 encodes a domain required for the function of mitochondrial cristae [39]. We also detected an AS switch in *PKM* (**Figure S2K**). This gene encodes pyruvate kinase M, an enzyme that catalyzes the final step in glycolysis. Exons 9 and 10 of *PKM* are mutually exclusive, giving rise to two isoforms with distinct metabolic roles: exon 9 inclusion produces PK-M1, an isoform predominantly expressed in terminally differentiated tissues with high oxidative demands, while exon 10 inclusion generates PK-M2, an isoform commonly found in proliferative fetal tissues and cancer [40]. Our finding that *PKM* exon 9 inclusion is higher in postnatal hearts compared to prenatal tissues and iPSC-CMs (**Figure S2K**) suggests that this splicing transition contributes to the

metabolic shift from glycolysis to oxidative phosphorylation during cardiac maturation after birth.

In summary, we identified numerous novel cardiac AS events that are regulated during the transition from pre- to postnatal life. These splicing alterations are predicted to affect critical cardiac functions, including extracellular matrix remodeling, sarcomere organization, transcriptional control, cell cycle regulation, and metabolic adaptation.

Heterogeneous mirroring of prenatal heart splicing regulation in iPSC-CMs

While the transition to postnatal life is a critical point for splicing regulation, splicing patterns during the prenatal period are not uniform across developmental stages. A comparison of early embryonic (4-5 weeks post-conception) and later fetal (18-19 weeks post-conception) heart samples revealed 568 alternative exon skipping events and 75 intron retention events (**Table S5**).

PCA analysis segregated embryonic and fetal hearts along PC2, with iPSC-CMs clustering between the two (**Figure S3A**). Embryonic hearts showed higher levels of exon skipping (**Figure 3A)** and intron retention (**Figure S3B**) compared to fetal hearts. Genes undergoing differential splicing during the embryonic to fetal transition were enriched in pathways related to muscle contraction, cell-cell communication, and VEGF signaling (**Figure 3B, Table S6**).

For example, *MYH14*, a critical gene in heart development [41], exhibited progressive exclusion of exon 6, which was highly included in embryonic hearts but almost completely skipped in fetal tissue and in iPSC-CMs (**Figure 3C**). This exon encodes part of the myosin motor domain, and its inclusion enhances actin-activated MgATPase activity and cell motility [42].

In another gene essential for heart development, *MYO18A* [43], exon 11, which also encodes part of the myosin motor domain, was completely excluded in fetal hearts but was partially included in embryonic hearts and iPSC-CMs (**Figure S3C**).

VEGFA exon 6, located in the heparin-binding domain, was more included in fetal compared to embryonic hearts (**Figure 3D**). In this case, iPSC-CMs mirrored earlier gestational stages (**Figure 3D**).

MBNL2 exon 6, which encodes a nuclear localization signal, showed higher inclusion in embryonic hearts compared to fetal hearts, while iPSC-CMs displayed an intermediate splicing pattern (**Figure 3E**).

EML1 exon 2, which encodes a motif thought to mediate interactions with microtubules and membranes, was more included in fetal hearts compared to embryonic hearts (**Figure 3F**). In this case, inclusion levels in iPSC-CMs were similar to fetal hearts. (**Figure 3F**).

Additional genes with significant regulation of prenatal splicing included *LAMA2*, *ANK3*, *ABI1*, *DCAF6*, *SLC25A3*, *ATP2B4* and *MYO5A* (**Figure S3D-J, Table S6**).

In conclusion, our findings demonstrate that cardiac splicing is dynamically regulated throughout prenatal development. While the splicing patterns observed in iPSC-CMs broadly resembled those of prenatal hearts, we identified variability in their degree of similarity depending on the specific splicing event. For some events, the inclusion levels in iPSC-CMs closely mirrored those of early embryonic hearts (**Figure 3D, E**), whereas other events aligned more closely with the splicing patterns observed in fetal hearts (**Figure 3C, F**). These observations suggest heterogeneity in the maturation state of iPSC-CMs relative to specific stages of prenatal heart development.

Maturation-driven splicing changes in iPSC-CMs recapitulate developmental transitions in the human heart

The observation that iPSC-CMs mimic prenatal heart splicing patterns but vary in their resemblance to specific developmental stages suggests heterogeneity in splicing trajectories during *in vitro* differentiation. To investigate this, we selected five splicing events for analysis by qRT-PCR at different stages of iPSC-CM maturation. We designed two experimental setups to assess how differentiation time and mechanical environment influence splicing regulation in iPSC-CMs. In one set of experiments, iPSC-CMs differentiated for 30 days were maintained in culture for an additional 10 days (**Figure 4A**). In another set of experiments, iPSC-CMs differentiated for 30 days were cultured for an additional 10 days on a micropatterned surface (**Figure 4A**). We analyzed cardiomyocytes derived from three independent iPSC lines,

performing three separate differentiation experiments for each line. As a hallmark of maturation, we assessed sarcomere length (**Figure 4B**). We observed a significant increase in sarcomere length between day 30 and day 40 (**Figure 4B**). Except for iPSC-CM C, culture on a micropatterned surface further increased the sarcomere length (**Figure 4B**).

For *TNNT2* exon 5, which increases calcium sensitivity and is predominantly included in prenatal hearts [44], we observed a reduction in inclusion levels at day 40 compared to day 30. Culturing iPSC-CMs on a micropatterned surface did not further influence exon 5 exclusion (**Figure 4C**).

In *CMYA5*, which encodes a protein required for cardiac dyad architecture [45], we identified novel exon skipping and intron retention events in prenatal hearts (**Figure S4A**) that are predicted to disrupt the reading frame and trigger nonsense-mediated decay. Consistent with this prediction, the levels of *CMYA5* mRNA were significantly reduced in prenatal hearts (**Figure S4B**). In hearts, inclusion of exon 5 increased progressively during prenatal development. In iPSC-CMs, we observed a similar trend, with exon 5 inclusion increasing between day 30 and day 40 of differentiation. This effect was particularly pronounced in cells cultured on a micropatterned surface (**Figure 4D**).

We identified several exons in the sarcomeric Z-line protein gene *LDB3* whose inclusion is developmentally regulated in the heart (**Figure 4E**, **Figure S4C-E**) [46]. Inclusion of exon 8 decreased progressively during prenatal development (**Figure 4E**). A significantly reduced inclusion of this exon was also observed in iPSC-CMs between day 30 and day 40, and this effect was more pronounced in iPSC-CMs cultured on micropatterned surfaces (**Figure 4E**).

For *TRDN*, a key regulator of calcium release [47], we identified a progressive increase in exon 19 inclusion during prenatal heart development (**Figure 4F**). A similar trend of increased inclusion was observed in iPSC-CMs between day 30 and day 40 (**Figure 4F**).

For *CAMK2D*, a gene involved in calcium handling and transcriptional regulation [48], exon 18 inclusion increased progressively during heart development (**Figure 4G**). Surprisingly, we detected little to no modulation of exon 18 inclusion in iPSC-CMs between day 30 and day 40, regardless of whether the cells were cultured on micropatterned surfaces (**Figure 4G**). These

findings suggest that the regulation of exon 18 inclusion in *CAMK2D* during development is not replicated in iPSC-CMs.

In conclusion, our results demonstrate that, despite inherent variability across iPSC lines and differentiation experiments, both temporal progression in culture and mechanical cues from micropatterned surfaces significantly influence splicing regulation. Except for *CAMK2D*, we observed a consistent trend of recapitulating the developmental splicing transitions characteristic of *in vivo* heart development.

A subset of splicing events distinguishes iPSC-CMs from hearts

In addition to *CAMK2D* exon 18, whose inclusion is developmentally regulated in the heart but remains largely unchanged during iPSC-CM maturation (**Figure 4G**), we identified a subset of splicing events that display distinct patterns in iPSC-CMs compared to human hearts, irrespective of developmental stage (**Figure 1J** - clusters 2 and 3**, Figure S1N** - cluster 2). Our analysis revealed 333 exons with splicing patterns unique to iPSC-CMs (**Table S7**). These iPSC-CM-specific splicing events may represent intrinsic developmental differences between iPSC-CMs and the native heart or could arise from variability introduced by the differentiation protocol. To clarify these possibilities, we expanded our analysis to include RNA-seq datasets generated from iPSC-derived cultures enriched for cardiomyocytes using metabolic selection with lactate (iPSC-CM C25) instead of fluorescence-activated cell sorting with antibodies to VCAM1 (iPSC-CM C, D, G, T) (see **Methods**).

Splicing events unique to iPSC-CMs were enriched in genes associated with striated muscle contraction and RNA metabolism, including splicing regulation (**Figure 5A**, **Table S8**). In heart tissue, the inclusion levels of *TPM1* exon 2, which encodes part of the tropomyosin domain, exceeded 94%. In contrast, inclusion levels were approximately 75% in iPSC-CMs D, G, and T, and around 88% in iPSC-CMs C25 (**Figure S5A**).

Among genes encoding splicing regulators, we found higher skipping of *CLK1* and *CLK4* exon 4 in iPSC-CMs derived using both protocols compared to heart tissue (**Figure 5B-C**). Exon 4 skipping produces truncated, catalytically inactive isoforms of these kinases [49]. A trend for increased exon 4 inclusion was observed during iPSC-CM maturation (**Figure 5B-C**). Significant

changes in exon 4 inclusion levels were further detected between iPSCs and iPSC-CMs (**Figure 5B-C**).

Increased skipping of *SNRPE* exon 2, which encodes part of the LSM domain required for spliceosome assembly, was also observed in iPSC-CMs derived using both protocols compared to heart tissue (**Figure 5D**). Interestingly, this exon was not dynamically regulated during iPSC differentiation or iPSC-CM maturation, suggesting that its altered splicing is an intrinsic feature of iPSCs.

In contrast, higher inclusion levels of splicing factor *RSRP1* exon 4 were observed in iPSC-CMs derived using both protocols compared to heart tissue (**Figure 5E**). Consistent with the prediction that inclusion of this exon disrupts the open reading frame and triggers NMD, *RSRP1* expression was lower in iPSC-CMs compared to heart tissue (**Figure S5B**).

Additionally, iPSC-CMs consistently displayed lower inclusion of exons that trigger nonsense-mediated decay (NMD) in mRNAs encoding several SR proteins, including *SRSF3* exon 4 [50], *SRSF6* exon 3 [51], and *TRA2B* exon 2 [52] (**Figure S5C-E**). We further observed reduced retention of *SRSF1* intron 3 and *SRSF5* intron 5 in iPSC-CMs compared to heart tissue (**Figure S5F-G**).

Beyond splicing regulators, we identified iPSC-CM-specific splicing patterns in genes involved in mRNA decay and modification. For example, inclusion of *UPF3A* exon 4, which encodes a domain required for interactions with the NMD machinery, is consistently lower in iPSC-CMs compared to heart tissue (**Figure 5F**). In the *PATL1* gene, inclusion of exon 7 is also lower in iPSC-CMs compared to heart tissue (**Figure S5H**). In the m6A methyltransferase *METTL3*, retention of intron 8 is consistently lower in iPSC-CMs compared to heart tissue (**Figure 5G**). Intron 8 retention disrupts the methylation domain, leading to a truncated, non-functional protein. Notably, *METTL3* splicing remained largely unchanged during iPSC differentiation and iPSC-CM maturation (**Figure 5G**).

Having identified dysregulated splicing in iPSC-CMs, we next explored changes in the expression of trans-acting splicing factors that could explain the observed alterations. Our analysis revealed a subset of mRNAs encoding splicing factors that were significantly downregulated in iPSC-CMs compared to pre- and postnatal hearts. These included SR protein kinases CLK1 and SRPK3, ELAVL3, ELAVL4 and NOVA2 (**Table S9**).

In summary, we identified a subset of unique splicing events that distinguish iPSC-CMs from native cardiac tissue. Despite some protocol-driven variability, most of the splicing patterns were consistent across iPSC-CMs generated with distinct differentiation methods.

DISCUSSION

In this study, we present a comprehensive characterization of AS dynamics during cardiomyocyte development *in vivo* and *in vitro*, and we highlight discrepancies in splicing regulation between iPSC-CMs and human hearts.

During pre- and postnatal development of the heart, cardiomyocytes undergo a maturation process that involves a wide spectrum of changes in cell structure, metabolism, function and gene expression [53]. Our comparative analysis of gene expression profiles showed that iPSC-CMs cluster more closely with prenatal heart tissue than postnatal hearts, in agreement with previous reports [54,55].

Alternative splicing (AS) is a critical post-transcriptional mechanism that regulates gene expression, affecting over 90% of human genes and allowing a single gene to generate multiple transcript variants with diverse functions [6,7]. To date, the best characterized examples of developmentally regulated cardiac alternative splicing have been shown to contribute to the extensive remodeling that the heart undergoes to meet the demands of increased workload during the transition from fetal to neonatal life and subsequently until adulthood [56–58]. For example, longer splicing isoforms of the sarcomeric protein titin are expressed in the fetus. These rapidly disappear after birth and are replaced by a smaller isoform that increases myocardial passive stiffness [59,60].

Despite recent progress, a comprehensive understanding of splicing regulation throughout human heart development remains incomplete. In our analysis, we identified the majority of alternative splicing events previously well-characterized as regulated during cardiac development *in vivo*. Furthermore, we show that splicing isoforms reported in the developing murine heart are conserved in the human heart (**Table S4**). Most important, we discovered novel splicing events that are differentially regulated between pre- and postnatal human hearts (**Table S4**). While some

of these events have been described in the context of disease, their regulation during normal heart development was previously unknown.

In addition to splicing differences between pre- and postnatal hearts, we identified novel splicing events that undergo regulation during prenatal life, between embryonic and fetal stages (**Table S6**). These events are enriched for involvement in pathways related to muscle contraction, cell-cell communication and signaling by VEGF, which is essential for vasculogenesis and angiogenesis during heart development [61].

Taken together, our findings offer an unprecedentedly detailed perspective on the temporal dynamics of splicing switches during human heart development, uncovering previously uncharted splicing programs that regulate cardiac maturation. Our analysis further shows that iPSC-CMs do not correspond to prenatal hearts at a specific gestational age based on their splicing profiles. Instead, splicing patterns in iPSC-CMs are heterogeneous, with some events resembling those found in early embryonic hearts, whereas others align more closely with later fetal stages. This variability highlights the heterogeneity in the maturation state of iPSC-CMs, reflecting their incomplete replication of *in vivo* cardiac development.

Additionally, we identified splicing events unique to iPSC-CMs, including exons that are consistently included in both pre- and postnatal hearts but frequently skipped in iPSC-CMs (**Table S8**). Notably, these iPSC-CM-specific splicing alterations include the mis-splicing of splicing regulators as well as factors involved in mRNA decay and modification. These combined splicing defects suggest widespread disruptions in RNA homeostasis, which may contribute to the functional immaturity of iPSC-CMs compared to native heart cells. This aligns with recent findings showing that the electrophysiological properties of stem cell-derived cardiomyocytes do not completely replicate those of native cardiomyocytes in prenatal human hearts [62].

Multiple splicing factors have been associated to cardiac splicing regulation. Namely, CELF and MBNL proteins are responsible for many splicing transitions that occur during mouse postnatal heart development [15,63]. The splicing factor SRSF1 also plays a critical role in maintaining specific splicing patterns during postnatal heart remodeling [64]. Additional RNA binding proteins involved in the regulation of alternative splicing events during heart development include *PTBP1* [65,66], *RBFOX2* [67], *SRSF5* [68], *SRSF10* [69], *RBM24* [70,71], *RBM20* [72,73] and *QKI* [74]. None of the

transcripts encoding these proteins was differentially expressed in iPSC-CMs (**Table S9**). However, we found that iPSC-CMs expressed significantly lower levels of *CLK1* and *SRPK3* mRNAs (**Table S9**), which encode members of two families of kinases that phosphorylate the serine/arginine-rich domain of SR splicing factors [49,75]. While the *CLK1* protein is ubiquitously expressed, *SRPK3* is specifically expressed in the developing heart and skeletal muscles [76]. Since SR protein phosphorylation modulates their activity as splicing factors [77,78], the combination of lower *CLK1* and *SRPK3* expression, along with the presence of a truncated, catalytically inactive *CLK1* isoform, may contribute to the aberrant splicing observed in iPSC-CMs.

Future studies are needed to determine the mechanisms leading to alternative splicing dysregulation in iPSC-CMs. Mis-splicing in iPSC-CMs can be caused by changes in the activity of splicing regulators that do not involve differential expression of the *cognate* mRNA. In this regard, two splicing proteins of the *CELF* family, *CELF1* and *CELF2*, were reported to be significantly down-regulated in the mouse heart after birth without a change in mRNA levels [15]. Notably, *CELF1* was shown to be stabilized by phosphorylation, which decreased in the postnatal heart [15].

In conclusion, our findings highlight the ability of iPSC-CMs to model key aspects of early heart development, while also revealing their limitations in recapitulating the full spectrum of splicing programs that govern cardiac maturation. The observed splicing immaturity and variability in iPSC-CMs underscore the need for further optimization of maturation protocols to more faithfully replicate native cardiac splicing transitions, ultimately enhancing their utility as robust *in vitro* models for cardiovascular research.

References

1. Buijtendijk, M.F.J., Barnett, P., and Van Den Hoff, M.J.B. (2020). Development of the human heart. American J of Med Genetics Pt C *184*, 7–22. https://doi.org/10.1002/ajmg.c.31778.

2. Luna-Zurita, L., Stirnimann, C.U., Glatt, S., Kaynak, B.L., Thomas, S., Baudin, F., Samee, M.A.H., He, D., Small, E.M., Mileikovsky, M., et al. (2016). Complex Interdependence Regulates Heterotypic Transcription Factor Distribution and Coordinates Cardiogenesis. Cell *164*, 999–1014. https://doi.org/10.1016/j.cell.2016.01.004.

3. Olson, E.N. (2006). Gene Regulatory Networks in the Evolution and Development of the Heart. Science *313*, 1922–1927. https://doi.org/10.1126/science.1132292.

4. Sylva, M., Van Den Hoff, M.J.B., and Moorman, A.F.M. (2014). Development of the human heart. American J of Med Genetics Pt A *164*, 1347–1371. https://doi.org/10.1002/ajmg.a.35896.

5. Meilhac, S.M., and Buckingham, M.E. (2018). The deployment of cell lineages that form the mammalian heart. Nat Rev Cardiol *15*, 705–724. https://doi.org/10.1038/s41569-018-0086-9.

6. Nilsen, T.W., and Graveley, B.R. (2010). Expansion of the eukaryotic proteome by alternative splicing. Nature *463*, 457–463. https://doi.org/10.1038/nature08909.

7. Wang, E.T., Sandberg, R., Luo, S., Khrebtukova, I., Zhang, L., Mayr, C., Kingsmore, S.F., Schroth, G.P., and Burge, C.B. (2008). Alternative isoform regulation in human tissue transcriptomes. Nature *456*, 470–476. https://doi.org/10.1038/nature07509.

8. Braunschweig, U., Barbosa-Morais, N.L., Pan, Q., Nachman, E.N., Alipanahi, B., Gonatopoulos-Pournatzis, T., Frey, B., Irimia, M., and Blencowe, B.J. (2014). Widespread intron retention in mammals functionally tunes transcriptomes. Genome Res. *24*, 1774–1786. https://doi.org/10.1101/gr.177790.114.

9. Kjer-Hansen, P., and Weatheritt, R.J. (2023). The function of alternative splicing in the proteome: rewiring protein interactomes to put old functions into new contexts. Nat Struct Mol Biol *30*, 1844–1856. https://doi.org/10.1038/s41594-023-01155-9.

10. Yang, X., Coulombe-Huntington, J., Kang, S., Sheynkman, G.M., Hao, T., Richardson, A., Sun, S., Yang, F., Shen, Y.A., Murray, R.R., et al. (2016). Widespread Expansion of Protein Interaction Capabilities by Alternative Splicing. Cell *164*, 805–817. https://doi.org/10.1016/j.cell.2016.01.029.

11. Baralle, F.E., and Giudice, J. (2017). Alternative splicing as a regulator of development and tissue identity. Nat Rev Mol Cell Biol *18*, 437–451. https://doi.org/10.1038/nrm.2017.27.

12. Blencowe, B.J. (2006). Alternative Splicing: New Insights from Global Analyses. Cell *126*, 37–47. https://doi.org/10.1016/j.cell.2006.06.023.

13. Merkin, J., Russell, C., Chen, P., and Burge, C.B. (2012). Evolutionary Dynamics of Gene and Isoform Regulation in Mammalian Tissues. Science *338*, 1593–1599. https://doi.org/10.1126/science.1228186.

14. Jimena Giudice, Giudice, J., Zheng Xia, Xia, Z., Eric T. Wang, Wang, E.T., Eric T. Wang, Marissa A. Scavuzzo, Scavuzzo, M.A., Amanda J. Ward, et al. (2014). Alternative splicing regulates vesicular trafficking genes in cardiomyocytes during postnatal heart development. Nature Communications *5*, 3603–3603. https://doi.org/10.1038/ncomms4603.

15. Kalsotra, A., Xiao, X., Ward, A.J., Castle, J.C., Johnson, J.M., Burge, C.B., and Cooper, T.A. (2008). A postnatal switch of CELF and MBNL proteins reprograms alternative splicing in the developing heart. Proc. Natl. Acad. Sci. U.S.A. *105*, 20333–20338. https://doi.org/10.1073/pnas.0809045105.

16. Van Den Hoogenhof, M.M.G., Pinto, Y.M., and Creemers, E.E. (2016). RNA Splicing: Regulation and Dysregulation in the Heart. Circ Res *118*, 454–468. https://doi.org/10.1161/CIRCRESAHA.115.307872.

17. Mazin, P.V., Khaitovich, P., Cardoso-Moreira, M., and Kaessmann, H. (2021). Alternative splicing during mammalian organ development. Nat Genet *53*, 925–934. https://doi.org/10.1038/s41588-021-00851-w.

18. Burridge, P.W., Sharma, A., and Wu, J.C. (2015). Genetic and Epigenetic Regulation of Human Cardiac Reprogramming and Differentiation in Regenerative Medicine. Annu. Rev. Genet. *49*, 461–484. https://doi.org/10.1146/annurev-genet-112414-054911.

19. Zaragoza, C., Gomez-Guerrero, C., Martin-Ventura, J.L., Blanco-Colio, L., Lavin, B., Mallavia, B., Tarin, C., Mas, S., Ortiz, A., and Egido, J. (2011). Animal Models of Cardiovascular Diseases. Journal of Biomedicine and Biotechnology *2011*, 1–13. https://doi.org/10.1155/2011/497841.

20. Takahashi, K., Tanabe, K., Ohnuki, M., Narita, M., Ichisaka, T., Tomoda, K., and Yamanaka, S. (2007). Induction of Pluripotent Stem Cells from Adult Human Fibroblasts by Defined Factors. Cell *131*, 861–872. https://doi.org/10.1016/j.cell.2007.11.019.

21. Karbassi, E., Fenix, A., Marchiano, S., Muraoka, N., Nakamura, K., Yang, X., and Murry, C.E. (2020). Cardiomyocyte maturation: advances in knowledge and implications for

regenerative medicine. Nat Rev Cardiol *17*, 341–359. https://doi.org/10.1038/s41569-019-0331-x.

22. Wang, J., An, M., Haubner, B.J., and Penninger, J.M. (2023). Cardiac regeneration: Options for repairing the injured heart. Front. Cardiovasc. Med. *9*, 981982. https://doi.org/10.3389/fcvm.2022.981982.

23. Cui, Y., Zheng, Y., Liu, X., Yan, L., Fan, X., Yong, J., Hu, Y., Dong, J., Li, Q., Wu, X., et al. (2019). Single-Cell Transcriptome Analysis Maps the Developmental Track of the Human Heart. Cell Reports *26*, 1934-1950.e5. https://doi.org/10.1016/j.celrep.2019.01.079.

24. Cao, J., O'Day, D.R., Pliner, H.A., Kingsley, P.D., Deng, M., Daza, R.M., Zager, M.A., Aldinger, K.A., Blecher-Gonen, R., Zhang, F., et al. (2020). A human cell atlas of fetal gene expression. Science *370*, eaba7721. https://doi.org/10.1126/science.aba7721.

25. Galdos, F.X., Lee, C., Lee, S., Paige, S., Goodyer, W., Xu, S., Samad, T., Escobar, G.V., Darsha, A., Beck, A., et al. (2023). Combined lineage tracing and scRNA-seq reveals unexpected first heart field predominance of human iPSC differentiation. eLife *12*, e80075. https://doi.org/10.7554/eLife.80075.

26. Tyser, R.C.V., Ibarra-Soria, X., McDole, K., Arcot Jayaram, S., Godwin, J., Van Den Brand, T.A.H., Miranda, A.M.A., Scialdone, A., Keller, P.J., Marioni, J.C., et al. (2021). Characterization of a common progenitor pool of the epicardium and myocardium. Science *371*, eabb2986. https://doi.org/10.1126/science.abb2986.

27. Cardoso-Moreira, M., Halbert, J., Valloton, D., Velten, B., Chen, C., Shao, Y., Liechti, A., Ascenção, K., Rummel, C., Ovchinnikova, S., et al. (2019). Gene expression across mammalian organ development. Nature *571*, 505–509. https://doi.org/10.1038/s41586-019-1338-5.

28. Schoenauer, R., Bertoncini, P., Machaidze, G., Aebi, U., Perriard, J.-C., Hegner, M., and Agarkova, I. (2005). Myomesin is a molecular spring with adaptable elasticity. J Mol Biol *349*, 367–379. https://doi.org/10.1016/j.jmb.2005.03.055.

29. Terenzi, F., and Ladd, A.N. (2010). Conserved developmental alternative splicing of muscleblind-like (MBNL) transcripts regulates MBNL localization and activity. RNA Biology *7*, 43–55. https://doi.org/10.4161/rna.7.1.10401.

30. Guo, W., Bharmal, S.J., Esbona, K., and Greaser, M.L. (2010). Titin Diversity—Alternative Splicing Gone Wild. Journal of Biomedicine and Biotechnology *2010*, 1–8. https://doi.org/10.1155/2010/753675.

31. LeWinter, M.M., and Granzier, H. (2010). Cardiac Titin: A Multifunctional Giant. Circulation *121*, 2137–2145. https://doi.org/10.1161/CIRCULATIONAHA.109.860171.

32. Efthymiou, G., Radwanska, A., Grapa, A.-I., Beghelli-de La Forest Divonne, S., Grall, D., Schaub, S., Hattab, M., Pisano, S., Poet, M., Pisani, D.F., et al. (2021). Fibronectin Extra Domains tune cellular responses and confer topographically distinct features to fibril networks. Journal of Cell Science *134*, jcs252957. https://doi.org/10.1242/jcs.252957.

33. Godbout, E., Son, D.O., Hume, S., Boo, S., Sarrazy, V., Clément, S., Kapus, A., Wehrle-Haller, B., Bruckner-Tuderman, L., Has, C., et al. (2020). Kindlin-2 Mediates Mechanical Activation of Cardiac Myofibroblasts. Cells *9*, 2702. https://doi.org/10.3390/cells9122702.

34. Timpl, R., Sasaki, T., Kostka, G., and Chu, M.-L. (2003). Fibulins: a versatile family of extracellular matrix proteins. Nat Rev Mol Cell Biol *4*, 479–489. https://doi.org/10.1038/nrm1130.

35. Gönczi, M., Teixeira, J.M.C., Barrera-Vilarmau, S., Mediani, L., Antoniani, F., Nagy, T.M., Fehér, K., Ráduly, Z., Ambrus, V., Tőzsér, J., et al. (2023). Alternatively spliced exon regulates context-dependent MEF2D higher-order assembly during myogenesis. Nat Commun *14*, 1329. https://doi.org/10.1038/s41467-023-37017-7.

36. Sun, X.-H., and Baltimore, D. (1991). An inhibitory domain of E12 transcription factor prevents DNA binding in E12 homodimers but not in E12 heterodimers. Cell *64*, 459–470. https://doi.org/10.1016/0092-8674(91)90653-G.

37. Yoneda-Kato, N., Tomoda, K., Umehara, M., Arata, Y., and Kato, J. (2005). Myeloid leukemia factor 1 regulates p53 by suppressing COP1 via COP9 signalosome subunit 3. EMBO J *24*, 1739–1749. https://doi.org/10.1038/sj.emboj.7600656.

38. John, G.B., Shang, Y., Li, L., Renken, C., Mannella, C.A., Selker, J.M.L., Rangell, L., Bennett, M.J., and Zha, J. (2005). The Mitochondrial Inner Membrane Protein Mitofilin Controls Cristae Morphology. MBoC *16*, 1543–1554. https://doi.org/10.1091/mbc.e04-08-0697.

39. Bock-Bierbaum, T., Funck, K., Wollweber, F., Lisicki, E., Von Der Malsburg, K., Von Der Malsburg, A., Laborenz, J., Noel, J.K., Hessenberger, M., Jungbluth, S., et al. (2022). Structural insights into crista junction formation by the Mic60-Mic19 complex. Sci. Adv. *8*, eabo4946. https://doi.org/10.1126/sciadv.abo4946.

40. Christofk, H.R., Vander Heiden, M.G., Harris, M.H., Ramanathan, A., Gerszten, R.E., Wei, R., Fleming, M.D., Schreiber, S.L., and Cantley, L.C. (2008). The M2 splice isoform of pyruvate kinase is important for cancer metabolism and tumour growth. Nature *452*, 230–233. https://doi.org/10.1038/nature06734.

41. Ma, X., Jana, S.S., Anne Conti, M., Kawamoto, S., Claycomb, W.C., and Adelstein, R.S. (2010). Ablation of Nonmuscle Myosin II-B and II-C Reveals a Role for Nonmuscle Myosin II in Cardiac Myocyte Karyokinesis. Mol Biol Cell *21*, 3952–3962. https://doi.org/10.1091/mbc.E10-04-0293.

42. Kim, K.-Y., Kovács, M., Kawamoto, S., Sellers, J.R., and Adelstein, R.S. (2005). Disease-associated Mutations and Alternative Splicing Alter the Enzymatic and Motile Activity of Nonmuscle Myosins II-B and II-C. Journal of Biological Chemistry *280*, 22769–22775. https://doi.org/10.1074/jbc.M503488200.

43. Horsthemke, M., Arnaud, C.-A., and Hanley, P.J. (2024). Are the class 18 myosins Myo18A and Myo18B specialist sarcomeric proteins? Front. Physiol. *15*, 1401717. https://doi.org/10.3389/fphys.2024.1401717.

44. Gomes, A.V., Guzman, G., Zhao, J., and Potter, J.D. (2002). Cardiac troponin T isoforms affect the Ca2+ sensitivity and inhibition of force development. Insights into the role of troponin T isoforms in the heart. J Biol Chem *277*, 35341–35349. https://doi.org/10.1074/jbc.M204118200.

45. Lu, F., Ma, Q., Xie, W., Liou, C.L., Zhang, D., Sweat, M.E., Jardin, B.D., Naya, F.J., Guo, Y., Cheng, H., et al. (2022). CMYA5 establishes cardiac dyad architecture and positioning. Nat Commun *13*, 2185. https://doi.org/10.1038/s41467-022-29902-4.

46. Huang, C., Zhou, Q., Liang, P., Hollander, M.S., Sheikh, F., Li, X., Greaser, M., Shelton, G.D., Evans, S., and Chen, J. (2003). Characterization and in Vivo Functional Analysis of Splice Variants of Cypher. Journal of Biological Chemistry *278*, 7360–7365. https://doi.org/10.1074/jbc.M211875200.

47. Chopra, N., and Knollmann, B.C. (2013). Triadin regulates cardiac muscle couplon structure and microdomain Ca2+ signalling: a path towards ventricular arrhythmias. Cardiovascular Research *98*, 187–191. https://doi.org/10.1093/cvr/cvt023.

48. Duran, J., Nickel, L., Estrada, M., Backs, J., and Van Den Hoogenhof, M.M.G. (2021). CaMKIIδ Splice Variants in the Healthy and Diseased Heart. Front. Cell Dev. Biol. *9*, 644630. https://doi.org/10.3389/fcell.2021.644630.

49. Colwill, K., Pawson, T., Andrews, B., Prasad, J., Manley, J.L., Bell, J.C., and Duncan, P.I. (1996). The Clk/Sty protein kinase phosphorylates SR splicing factors and regulates their intranuclear distribution. EMBO J *15*, 265–275.

50. Jumaa, H. (1997). The splicing factor SRp20 modifies splicing of its own mRNA and ASF/SF2 antagonizes this regulation. The EMBO Journal *16*, 5077–5085. https://doi.org/10.1093/emboj/16.16.5077.

51. de Oliveira Freitas Machado, C., Schafranek, M., Brüggemann, M., Hernández Cañás, M.C., Keller, M., Di Liddo, A., Brezski, A., Blümel, N., Arnold, B., Bremm, A., et al. (2023). Poison cassette exon splicing of *SRSF6* regulates nuclear speckle dispersal and the response to hypoxia. Nucleic Acids Research *51*, 870–890. https://doi.org/10.1093/nar/gkac1225.

52. Akaike, Y., Masuda, K., Kuwano, Y., Nishida, K., Kajita, K., Kurokawa, K., Satake, Y., Shoda, K., Imoto, I., and Rokutan, K. (2014). HuR Regulates Alternative Splicing of the *TRA2* β Gene in Human Colon Cancer Cells under Oxidative Stress. Molecular and Cellular Biology *34*, 2857–2873. https://doi.org/10.1128/MCB.00333-14.

53. Guo, Y., and Pu, W.T. (2020). Cardiomyocyte Maturation: New Phase in Development. Circulation Research *126*, 1086–1106. https://doi.org/10.1161/CIRCRESAHA.119.315862.

54. Synnergren, J., Améen, C., Jansson, A., and Sartipy, P. (2012). Global transcriptional profiling reveals similarities and differences between human stem cell-derived cardiomyocyte clusters and heart tissue. Physiological Genomics *44*, 245–258. https://doi.org/10.1152/physiolgenomics.00118.2011.

55. Van Den Berg, C.W., Okawa, S., Chuva De Sousa Lopes, S.M., Van Iperen, L., Passier, R., Braam, S.R., Tertoolen, L.G., Del Sol, A., Davis, R.P., and Mummery, C.L. (2015). Transcriptome of human foetal heart compared with cardiomyocytes from pluripotent stem cells. Development, dev.123810. https://doi.org/10.1242/dev.123810.

56. Giudice, J., and Cooper, T.A. (2014). RNA-Binding Proteins in Heart Development. In Systems Biology of RNA Binding Proteins Advances in Experimental Medicine and Biology., G. W. Yeo, ed. (Springer New York), pp. 389–429. https://doi.org/10.1007/978-1-4939-1221-6_11.

57. Li, Z., Cao, C., Zhao, Q., Li, D., Han, Y., Zhang, M., Mao, L., Zhou, B., and Wang, L. (2024). RNA splicing controls organ-wide maturation of postnatal heart in mice. Developmental Cell *0*. https://doi.org/10.1016/j.devcel.2024.09.018.

58. Weeland, C.J., Van Den Hoogenhof, M.M., Beqqali, A., and Creemers, E.E. (2015). Insights into alternative splicing of sarcomeric genes in the heart. Journal of Molecular and Cellular Cardiology *81*, 107–113. https://doi.org/10.1016/j.yjmcc.2015.02.008.

59. Lahmers, S., Wu, Y., Call, D.R., Labeit, S., and Granzier, H. (2004). Developmental control of titin isoform expression and passive stiffness in fetal and neonatal myocardium. Circ Res *94*, 505–513. https://doi.org/10.1161/01.RES.0000115522.52554.86.

60. Opitz, C.A., Leake, M.C., Makarenko, I., Benes, V., and Linke, W.A. (2004). Developmentally regulated switching of titin size alters myofibrillar stiffness in the

perinatal heart. Circ Res *94*, 967–975. https://doi.org/10.1161/01.RES.0000124301.48193.E1.

61. Lambrechts, D., and Carmeliet, P. (2004). Genetics in Zebrafish, Mice, and Humans to Dissect Congenital Heart Disease: Insights in the Role of VEGF. In Current Topics in Developmental Biology (Elsevier), pp. 189–224. https://doi.org/10.1016/S0070-2153(04)62007-2.

62. Grubb, S., Vestergaard, M.L., Andersen, A.S., Rasmussen, K.K., Mamsen, L.S., Tuckute, G., Grunnet-Lauridsen, K., Møllgård, K., Ernst, E., Christensen, S.T., et al. (2019). Comparison of Cultured Human Cardiomyocyte Clusters Obtained from Embryos/Fetuses or Derived from Human Embryonic Stem Cells. Stem Cells and Development *28*, 608–619. https://doi.org/10.1089/scd.2018.0231.

63. Wang, E.T., Cody, N.A.L., Jog, S., Biancolella, M., Wang, T.T., Treacy, D.J., Luo, S., Schroth, G.P., Housman, D.E., Reddy, S., et al. (2012). Transcriptome-wide Regulation of Pre-mRNA Splicing and mRNA Localization by Muscleblind Proteins. Cell *150*, 710–724. https://doi.org/10.1016/j.cell.2012.06.041.

64. Xu, X., Yang, D., Ding, J.-H., Wang, W., Chu, P.-H., Dalton, N.D., Wang, H.-Y., Bermingham, J.R., Ye, Z., Liu, F., et al. (2005). ASF/SF2-regulated CaMKIIdelta alternative splicing temporally reprograms excitation-contraction coupling in cardiac muscle. Cell *120*, 59–72. https://doi.org/10.1016/j.cell.2004.11.036.

65. Cao, J., Routh, A.L., and Kuyumcu-Martinez, M.N. (2021). Nanopore sequencing reveals full-length Tropomyosin 1 isoforms and their regulation by RNA-binding proteins during rat heart development. J Cell Mol Med *25*, 8352–8362. https://doi.org/10.1111/jcmm.16795.

66. Charlet-B, N., Singh, G., Cooper, T.A., and Logan, P. (2002). Dynamic Antagonism between ETR-3 and PTB Regulates Cell Type-Specific Alternative Splicing. Molecular Cell *9*, 649–658. https://doi.org/10.1016/S1097-2765(02)00479-3.

67. Verma, S.K., Deshmukh, V., Thatcher, K., Belanger, K.K., Rhyner, A.M., Meng, S., Holcomb, R.J., Bressan, M., Martin, J.F., Cooke, J.P., et al. (2022). RBFOX2 is required for establishing RNA regulatory networks essential for heart development. Nucleic Acids Res *50*, 2270–2286. https://doi.org/10.1093/nar/gkac055.

68. Zhang, X., Wang, Z., Xu, Q., Chen, Y., Liu, W., Zhong, T., Li, H., Quan, C., Zhang, L., and Cui, C.-P. (2021). Splicing factor Srsf5 deletion disrupts alternative splicing and causes noncompaction of ventricular myocardium. iScience *24*, 103097. https://doi.org/10.1016/j.isci.2021.103097.

69. Feng, Y., Valley, M.T., Lazar, J., Yang, A.L., Bronson, R.T., Firestein, S., Coetzee, W.A., and Manley, J.L. (2009). SRp38 regulates alternative splicing and is required for Ca(2+) handling in the embryonic heart. Dev Cell *16*, 528–538. https://doi.org/10.1016/j.devcel.2009.02.009.

70. Poon, K.L., Tan, K.T., Wei, Y.Y., Ng, C.P., Colman, A., Korzh, V., and Xu, X.Q. (2012). RNA-binding protein RBM24 is required for sarcomere assembly and heart contractility. Cardiovasc Res *94*, 418–427. https://doi.org/10.1093/cvr/cvs095.

71. Yang, J., Hung, L.-H., Licht, T., Kostin, S., Looso, M., Khrameeva, E., Bindereif, A., Schneider, A., and Braun, T. (2014). RBM24 is a major regulator of muscle-specific alternative splicing. Dev Cell *31*, 87–99. https://doi.org/10.1016/j.devcel.2014.08.025.

72. Guo, W., Schafer, S., Greaser, M.L., Radke, M.H., Liss, M., Govindarajan, T., Maatz, H., Schulz, H., Li, S., Parrish, A.M., et al. (2012). RBM20, a gene for hereditary cardiomyopathy, regulates titin splicing. Nat Med *18*, 766–773. https://doi.org/10.1038/nm.2693.

73. Li, S., Guo, W., Dewey, C.N., and Greaser, M.L. (2013). Rbm20 regulates titin alternative splicing as a splicing repressor. Nucleic Acids Res *41*, 2659–2672. https://doi.org/10.1093/nar/gks1362.

74. Montañés-Agudo, P., Aufiero, S., Schepers, E.N., van der Made, I., Pinto, Y.M., and Creemers, E. (2022). The RNA-binding protein QKI governs a muscle-specific alternative splicing program that shapes the contractile function of cardiomyocytes. Journal of Molecular and Cellular Cardiology *173*, S161. https://doi.org/10.1016/j.yjmcc.2022.08.317.

75. Zhong, X.-Y., Ding, J.-H., Adams, J.A., Ghosh, G., and Fu, X.-D. (2009). Regulation of SR protein phosphorylation and alternative splicing by modulating kinetic interactions of SRPK1 with molecular chaperones. Genes Dev. *23*, 482–495. https://doi.org/10.1101/gad.1752109.

76. Nakagawa, O., Arnold, M., Nakagawa, M., Hamada, H., Shelton, J.M., Kusano, H., Harris, T.M., Childs, G., Campbell, K.P., Richardson, J.A., et al. (2005). Centronuclear myopathy in mice lacking a novel muscle-specific protein kinase transcriptionally regulated by MEF2. Genes Dev. *19*, 2066–2077. https://doi.org/10.1101/gad.1338705.

77. Fedorov, O., Huber, K., Eisenreich, A., Filippakopoulos, P., King, O., Bullock, A.N., Szklarczyk, D., Jensen, L.J., Fabbro, D., Trappe, J., et al. (2011). Specific CLK Inhibitors from a Novel Chemotype for Regulation of Alternative Splicing. Chemistry & Biology *18*, 67–76. https://doi.org/10.1016/j.chembiol.2010.11.009.

78. Keshwani, M.M., Aubol, B.E., Fattet, L., Ma, C.-T., Qiu, J., Jennings, P.A., Fu, X.-D., and Adams, J.A. (2015). Conserved proline-directed phosphorylation regulates SR protein conformation and splicing function. Biochemical Journal *466*, 311–322. https://doi.org/10.1042/BJ20141373.

79. Yu, J., Hu, K., Smuga-Otto, K., Tian, S., Stewart, R., Slukvin, I.I., and Thomson, J.A. (2009). Human Induced Pluripotent Stem Cells Free of Vector and Transgene Sequences. Science *324*, 797–801. https://doi.org/10.1126/science.1172482.

80. Burridge, P.W., Matsa, E., Shukla, P., Lin, Z.C., Churko, J.M., Ebert, A.D., Lan, F., Diecke, S., Huber, B., Mordwinkin, N.M., et al. (2014). Chemically defined generation of human cardiomyocytes. Nat Methods *11*, 855–860. https://doi.org/10.1038/nmeth.2999.

81. Knight, W.E., Cao, Y., Lin, Y.-H., Chi, C., Bai, B., Sparagna, G.C., Zhao, Y., Du, Y., Londono, P., Reisz, J.A., et al. (2021). Maturation of Pluripotent Stem Cell-Derived Cardiomyocytes Enables Modeling of Human Hypertrophic Cardiomyopathy. Stem Cell Reports *16*, 519–533. https://doi.org/10.1016/j.stemcr.2021.01.018.

82. Silva, T.P., Bekman, E.P., Fernandes, T.G., Vaz, S.H., Rodrigues, C.A.V., Diogo, M.M., Cabral, J.M.S., and Carmo-Fonseca, M. (2020). Maturation of Human Pluripotent Stem Cell-Derived Cerebellar Neurons in the Absence of Co-culture. Front. Bioeng. Biotechnol. *8*, 70. https://doi.org/10.3389/fbioe.2020.00070.

83. Moretti, A., Bellin, M., Welling, A., Jung, C.B., Lam, J.T., Bott-Flügel, L., Dorn, T., Goedel, A., Höhnke, C., Hofmann, F., et al. (2010). Patient-Specific Induced Pluripotent Stem-Cell Models for Long-QT Syndrome. N Engl J Med *363*, 1397–1409. https://doi.org/10.1056/NEJMoa0908679.

84. Jager, J., Ribeiro, M., Furtado, M., Carvalho, T., Syrris, P., Lopes, L.R., Elliott, P.M., Cabral, J.M.S., Carmo-Fonseca, M., Da Rocha, S.T., et al. (2024). Patient-derived induced pluripotent stem cells to study non-canonical splicing variants associated with Hypertrophic Cardiomyopathy. Stem Cell Research *81*, 103582. https://doi.org/10.1016/j.scr.2024.103582.

85. Breckwoldt, K., Letuffe-Brenière, D., Mannhardt, I., Schulze, T., Ulmer, B., Werner, T., Benzin, A., Klampe, B., Reinsch, M.C., Laufer, S., et al. (2017). Differentiation of cardiomyocytes and generation of human engineered heart tissue. Nat Protoc *12*, 1177–1197. https://doi.org/10.1038/nprot.2017.033.

86. Radke, M.H., Badillo-Lisakowski, V., Britto-Borges, T., Kubli, D.A., Jüttner, R., Parakkat, P., Carballo, J.L., Hüttemeister, J., Liss, M., Hansen, A., et al. (2021). Therapeutic inhibition of RBM20 improves diastolic function in a murine heart failure model and

human engineered heart tissue. Sci. Transl. Med. *13*, eabe8952. https://doi.org/10.1126/scitranslmed.abe8952.

87. Warren, C.M., Krzesinski, P.R., and Greaser, M.L. (2003). Vertical agarose gel electrophoresis and electroblotting of high-molecular-weight proteins. Electrophoresis *24*, 1695–1702. https://doi.org/10.1002/elps.200305392.

88. Melsted, P., Booeshaghi, A.S., Liu, L., Gao, F., Lu, L., Min, K.H., Da Veiga Beltrame, E., Hjörleifsson, K.E., Gehring, J., and Pachter, L. (2021). Modular, efficient and constant-memory single-cell RNA-seq preprocessing. Nat Biotechnol *39*, 813–818. https://doi.org/10.1038/s41587-021-00870-2.

89. Hao, Y., Hao, S., Andersen-Nissen, E., Mauck, W.M., Zheng, S., Butler, A., Lee, M.J., Wilk, A.J., Darby, C., Zager, M., et al. (2021). Integrated analysis of multimodal single-cell data. Cell *184*, 3573-3587.e29. https://doi.org/10.1016/j.cell.2021.04.048.

90. participants in the 1st Human Cell Atlas Jamboree, Lun, A.T.L., Riesenfeld, S., Andrews, T., Dao, T.P., Gomes, T., and Marioni, J.C. (2019). EmptyDrops: distinguishing cells from empty droplets in droplet-based single-cell RNA sequencing data. Genome Biol *20*, 63. https://doi.org/10.1186/s13059-019-1662-y.

91. Mercer, T.R., Neph, S., Dinger, M.E., Crawford, J., Smith, M.A., Shearwood, A.-M.J., Haugen, E., Bracken, C.P., Rackham, O., Stamatoyannopoulos, J.A., et al. (2011). The Human Mitochondrial Transcriptome. Cell *146*, 645–658. https://doi.org/10.1016/j.cell.2011.06.051.

92. Wu, T., Hu, E., Xu, S., Chen, M., Guo, P., Dai, Z., Feng, T., Zhou, L., Tang, W., Zhan, L., et al. (2021). clusterProfiler 4.0: A universal enrichment tool for interpreting omics data. The Innovation *2*, 100141. https://doi.org/10.1016/j.xinn.2021.100141.

93. Carlson, M. (2017). org.Hs.eg.db. (Bioconductor). https://doi.org/10.18129/B9.BIOC.ORG.HS.EG.DB https://doi.org/10.18129/B9.BIOC.ORG.HS.EG.DB.

94. Andrews S (2010). FastQC: A Quality Control Tool for High Throughput Sequence Data.

95. Krueger, F., James, F., Ewels, P., Afyounian, E., and Schuster-Boeckler, B. (2021). FelixKrueger/TrimGalore: v0.6.7 - DOI via Zenodo. Version 0.6.7 (Zenodo). https://doi.org/10.5281/ZENODO.5127899 https://doi.org/10.5281/ZENODO.5127899.

96. Patro, R., Duggal, G., Love, M.I., Irizarry, R.A., and Kingsford, C. (2017). Salmon provides fast and bias-aware quantification of transcript expression. Nat Methods *14*, 417–419. https://doi.org/10.1038/nmeth.4197.

97. Dobin, A., Davis, C.A., Schlesinger, F., Drenkow, J., Zaleski, C., Jha, S., Batut, P., Chaisson, M., and Gingeras, T.R. (2013). STAR: ultrafast universal RNA-seq aligner. Bioinformatics *29*, 15–21. https://doi.org/10.1093/bioinformatics/bts635.

98. Li, H., Handsaker, B., Wysoker, A., Fennell, T., Ruan, J., Homer, N., Marth, G., Abecasis, G., Durbin, R., and 1000 Genome Project Data Processing Subgroup (2009). The Sequence Alignment/Map format and SAMtools. Bioinformatics *25*, 2078–2079. https://doi.org/10.1093/bioinformatics/btp352.

99. Frankish, A., Diekhans, M., Ferreira, A.-M., Johnson, R., Jungreis, I., Loveland, J., Mudge, J.M., Sisu, C., Wright, J., Armstrong, J., et al. (2019). GENCODE reference annotation for the human and mouse genomes. Nucleic Acids Research *47*, D766–D773. https://doi.org/10.1093/nar/gky955.

100. R Core Team (2021). R: A language and environment for statistical computing. (R Foundation for Statistical Computing, Vienna, Austria.).

101. Soneson, C., Love, M.I., and Robinson, M.D. (2016). Differential analyses for RNA-seq: transcript-level estimates improve gene-level inferences. F1000Res *4*, 1521. https://doi.org/10.12688/f1000research.7563.2.

102. Wei, Taiyun and Simko, Viktor R package “corrplot”: Visualization of a Correlation Matrix.

103. Chen, H., and Boutros, P.C. (2011). VennDiagram: a package for the generation of highly-customizable Venn and Euler diagrams in R. BMC Bioinformatics *12*, 35. https://doi.org/10.1186/1471-2105-12-35.

104. Love, M.I., Huber, W., and Anders, S. (2014). Moderated estimation of fold change and dispersion for RNA-seq data with DESeq2. Genome Biol *15*, 550. https://doi.org/10.1186/s13059-014-0550-8.

105. Wickham, H. (2016). ggplot2 (Springer International Publishing) https://doi.org/10.1007/978-3-319-24277-4.

106. Suzuki, R., and Shimodaira, H. (2006). Pvclust: an R package for assessing the uncertainty in hierarchical clustering. Bioinformatics *22*, 1540–1542. https://doi.org/10.1093/bioinformatics/btl117.

107. Newman, A.M., Steen, C.B., Liu, C.L., Gentles, A.J., Chaudhuri, A.A., Scherer, F., Khodadoust, M.S., Esfahani, M.S., Luca, B.A., Steiner, D., et al. (2019). Determining cell type abundance and expression from bulk tissues with digital cytometry. Nat Biotechnol *37*, 773–782. https://doi.org/10.1038/s41587-019-0114-2.

108. Shen, S., Park, J.W., Lu, Z., Lin, L., Henry, M.D., Wu, Y.N., Zhou, Q., and Xing, Y. (2014). rMATS: Robust and flexible detection of differential alternative splicing from replicate RNA-Seq data. Proc. Natl. Acad. Sci. U.S.A. *111*. https://doi.org/10.1073/pnas.1419161111.

109. Vaquero-Garcia, J., Aicher, J.K., Jewell, S., Gazzara, M.R., Radens, C.M., Jha, A., Norton, S.S., Lahens, N.F., Grant, G.R., and Barash, Y. (2023). RNA splicing analysis using heterogeneous and large RNA-seq datasets. Nat Commun *14*, 1230. https://doi.org/10.1038/s41467-023-36585-y.

110. Tapial, J., Ha, K.C.H., Sterne-Weiler, T., Gohr, A., Braunschweig, U., Hermoso-Pulido, A., Quesnel-Vallières, M., Permanyer, J., Sodaei, R., Marquez, Y., et al. (2017). An atlas of alternative splicing profiles and functional associations reveals new regulatory programs and genes that simultaneously express multiple major isoforms. Genome Res. *27*, 1759–1768. https://doi.org/10.1101/gr.220962.117.

111. Kolde R (2019). pheatmap: Pretty Heatmaps.

112. Neuwirth E (2014). RColorBrewer: ColorBrewer Palettes.

113. Garrido-Martín, D., Palumbo, E., Guigó, R., and Breschi, A. (2018). ggsashimi: Sashimi plot revised for browser- and annotation-independent splicing visualization. PLoS Comput Biol *14*, e1006360. https://doi.org/10.1371/journal.pcbi.1006360.

114. Louadi, Z., Elkjaer, M.L., Klug, M., Lio, C.T., Fenn, A., Illes, Z., Bongiovanni, D., Baumbach, J., Kacprowski, T., List, M., et al. (2021). Functional enrichment of alternative splicing events with NEASE reveals insights into tissue identity and diseases. Genome Biol *22*, 327. https://doi.org/10.1186/s13059-021-02538-1.

Methods

Human iPSCs

In this study, the following human iPSC lines were used. The DF6.9.9 T.B cell line, provided by the WiCell Bank (https://www.wicell.org/) was reprogrammed from male foreskin fibroblasts [79], and is here referred to as iPSC-D. The Gibco® Human Episomal iPSC line (iPSC6.2), here referred to as iPSC-G, was derived from female CD34+ cord blood cells [80]. The Cuso-2 iPSC line, here referred as iPSC-C, was reprogrammed from skin fibroblasts of a healthy male donor [81]. The cell line F002.1A.13, here referred to as iPSC-T, was derived from skin fibroblasts of a healthy female donor [82]. The hiPSC C25 line was a gift from A. Moretti, Munich, Germany [83].

Cardiomyocyte differentiation

Cardiomyocytes differentiated from iPSC lines D, G, T and G were generated as previously described [84]. On day 13 of differentiation, cellular aggregates were dissociated using 0,25% Trypsin-EDTA (Gibco) for 7 min at 37ºC. After dissociation, cells were washed with 2% fetal bovine serum (FBS) and 2mM EDTA in phosphate buffered saline (PBS, 0.1M), and incubated with VCAM1 antibody (BioLegend, 1:50) diluted in PBS/2% FBS for 15 min at 4ºC. Then, cells were washed and suspended in PBS/2% FBS for FACS sorting (BD FACSAria™ III Cell Sorter) using a 100µm nozzle at 4ºC. Purified VCAM1 positive cells were plated on wells coated with Matrigel, at a seeding density between 20,000 – 40,000 cells/cm2. Alternatively, cardiomyocytes were differentiated from the iPSC C25 line, as described [85,86].

iPSC-CM culture on a micropatterned surface

On day 30 of differentiation, iPSC-CMs were replated by incubating with 0,25% Trypsin-EDTA (Gibco) for 3 min at 37ºC, followed by trypsin neutralization using PBS supplemented with 10% FBS. Cells were cultured on micropatterned coverslips (4Dcell, 10mmx10mm, 100 µm pattern) for an additional 10 days. The RPMI + B27 medium was replaced every 2 days and at day 40 of

differentiation coverslips were fixed in 3.7% PFA and iPSC-CMs were collected in NZYol (NZYTech®) for subsequent RNA analysis.

Fluorescence microscopy and image analysis

Immunofluorescence was performed as previously described [84] using a mouse anti-myosin-binding protein C antibody (Santa Cruz Biotechnology, sc-131781), a rabbit anti-α-actinin antibody (Abcam, ab9465) and Alexa Fluor™ 546 phalloidin for actin staining. Fluorescence images were acquired with Zeiss LSM 710 Confocal Laser Point-Scanning Microscope. Quantitative image analysis was performed using ImageJ (https://imagej.nih.gov/) standard plugins. For sarcomere length measurements, statistical analysis was performed using Brown-Forsythe and Welch ANOVA tests to account for unequal variances, followed by Games-Howell's multiple comparisons test.

Quantitative RT-PCR (qRT-PCR)

Total RNA was extracted using NZYol (NZYTech®) and digested with DNase I (Roche®). cDNA synthesis was performed the SuperScript IV Reverse Transcriptase (Invitrogen™) with oligodT primers. qRT-PCR was carried out using the Universal SYBR Green Supermix (Bio-Rad) and specific primers designed for the selected splicing events (listed in **Table S10**). Each PCR reactions was run in triplicate, using the ViiA™7 RT-PCR Systems (Applied BioSystems). Quantification was performed using the 2–ΔCt method. The level of the target exon was normalized to the level of a constitutive exon from the same gene (i.e., an exon that is consistently included in all splicing isoforms transcribed from the gene). For statistical analysis we used Brown-Forsythe and Welch ANOVA tests to account for unequal variances, followed by Games-Howell's multiple comparisons test.

Analysis of titin isoform expression

Titin protein isoforms were detected by agarose gel electrophoresis, as described previously [87].

Single-cell RNA sequencing

At day 30, differentiated cells were dissociated using 0.25% Trypsin-EDTA (Gibco) for 5 min at 37ºC. After stopping the reaction, dissociated cells were resuspended in PBS/0.1% bovine serum albumin (BSA; Life Technologies), filtered through a 100 µm pore filter and stored in ice. Cell viability was assessed by manual counting using Trypan Blue. Viable cell suspensions (1x106 cells/mL) were partitioned into Gel Beads-in-emulsion (GEMs), in order to capture approximately 10000 cells in single cell droplets, using the Chromium Single Cell 3′ GEM, Library & Gel Bead Kit (version 3, 10X Genomics, PN-1000092) and Chromium Single Cell B Chip Kit (10X Genomics, PN-1000074). Barcoded cDNA was extracted from the GEMs by Post-GEM RT-cleanup, PCR amplified and subjected to quality control and quantification. Single Cell 3′ Gene Expression libraries from single cells was then performed using Chromium i7 Multiplex Kit (PN-120262). All the steps were performed according to the manufacturer's protocol. Libraries were sequenced using an Illumina NextSeq 500 Instrument with a 300 cycles kit. The raw FASTQ files have been uploaded to ArrayExpress and can be accessed using the accession number E-MTAB-13850.

Single-cell RNA sequencing analysis

Raw sequencing reads from FASTQ files were pseudo-aligned to the transcriptome using Kallisto BUStools [88]. The resulting count matrix was imported into R and converted into a Seurat object using Seurat v.5.1.0 [89]. To retain high-quality cell-containing droplets, emptyDrops from DropletUtils v1.24.0 [90] was used with a false discovery rate (FDR) of ≤ 0.01. Cells were filtered according to their number of expressed genes (≥ 500), number of UMIs (≥ 1000), log10GenesPerUMI (> 0.8) and ribosomal ratio (> 0.05). The threshold for the expression of mitochondrial genes was set to 40% given the high energy needs of cardiomyocytes [91]. We further kept only those genes expressed in more than 10 cells in each sample. Counts were normalized, adjusted for variance, and the 1000 most highly variable features were identified using the SCTransform function, while regressing out sequencing depth effects. Principal component analysis was performed on these features and the five principal components

explaining the most variance were used for UMAP dimensionality reduction and to build a SNN graph. Known cardiomyocyte markers were used to select an appropriate resolution that allows to capture this cell population. Clustering was done using FindClusters function, with the Louvain algorithm with multilevel refinement, and resolution set to 0.01 for iPSC-CM_T and 0.05 for iPSC-CM_D. Doublet detection and removal were performed using DoubletFinder v.2.0.4 with the first 5 principal components (PCs) and pK = 0.07 for iPSC-CM_T and pK = 0.05 for iPSC-CM_D. Cluster markers were identified using Wilcoxon's rank sum test implemented in FindAllMarkers function. We considered only positive markers, as well as genes detected in at least 25% of the cells of each population, and with a minimum log2FC of 0.5. Markers with an adjusted p-value ≤ 0.01 were ranked by $\log_2$FC and used for gene set enrichment analysis (GSEA) with gseGO function of clusterProfiler 4.12.6 [92] and org.Hs.eg.db v.3.16.0 [93]. For automated cell type classification, label transfer was performed using Seurat's FindTransferAnchors and TransferData functions, using the first 25 PCs of Cui *et al.* dataset [23], according to the study methodology. Only cells assignments with a prediction score higher than 0.6 were kept.

Bulk RNA-sequencing

RNA was extracted using NZYol (NZYTech®) and digested with DNase I (Roche®). At least 1µg of total RNA was obtained from each culture of iPSC-CMs at day 30 of differentiation. After purification with poly-T oligo-attached magnetic beads, libraries were prepared using the NEBNext® Ultra™ Directional RNA Library Prep Kit, and sequenced on the Illumina platform Novaseq6000. The raw FASTQ files have been uploaded to ArrayExpress and can be accessed using the accession number E-MTAB-13757 [27].

Additionally, we used RNA sequencing data from 50 healthy human hearts - 38 prenatal and 12 postnatal, generated in a previous study. Raw data (FASTQ files) was downloaded from ArrayExpress (https://www.ebi.ac.uk/arrayexpress/), with the accession number E-MTAB-6814 39.

Data preprocessing, genome alignment and transcript quantification

Quality control of the sequenced reads was performed using *FastQC v0.11.5* [94]. Adaptors, low-quality bases (Phred quality <20) and reads shorter than 75bp were filtered out using *Trimgalore v0.6.4* [95]. Filtered reads were pseudo-aligned to the human transcriptome and bootstrapped transcript abundance was estimated with *Salmon v1.10.2* [96], with default parameters, 100 resamplings, fragment length distribution set to a mean of 100 bp and standard deviation of 10 bp, and correction for GC and sequencing bias. Trimmed reads were also mapped to the human reference genome (GRCh38/hg38) using the splice-aware aligner *STAR v2.7.10b* [97]. Chimeric alignments were detected (--chimSegmentMin 20), splice junctions were optimized with --sjdbOverhang 99, and two-pass mapping (--twopassMode Basic) was used to improve splice junction detection. Only uniquely mapped reads were kept using *samtools v.1.7* [98]. GENCODE v45 human primary gene annotation was used as reference [99]. **Table S1** summarizes the main biological and technical characteristics of all the samples.

Gene expression analysis

Transcriptomic analysis was performed using R *v4.4.1* software [100]. Prior to further analysis, data was filtered so that only genes with more than 10 read counts in at least three samples were kept. Transcript read counts were converted into a gene-level count matrix using *tximport v1.32.0* [101]. To filter out lowly expressed genes that could possibly result from transcriptional noise, only genes with transcripts per million (TPM) > 1 were considered. This threshold was determined based on the read counts distribution observed with a log10(TPM) histogram. Pearson pairwise correlation coefficients (r) were computed on rlog-transformed counts to assess the similarity between samples. The correlation matrix was visualized using *corrplot v0.*94 [102]. Venn diagrams illustrating the overlap of expressed genes (TPM > 1) between different iPSC-CM lines were generated using *VennDiagram v1.7.3* [103]. To prevent highly expressed genes from dominating the analysis, counts were transformed using varianceStabilizingTransformation (VST) from *DESeq2 v1.44.0* [104]. Principal component analysis (PCA) was performed on transformed read counts to discern the main sources of variation in the dataset using *ggplot2 v3.5.1* [105]. Regular hierarchical clustering dendrograms were drawn using the R base function hclust with average linkage clustering and 1-pairwise Spearman correlation coefficients as the distance metric. The

pvclust v2.2-0 [106] package was used to assess the uncertainty of the clustering and to compute p-values for each cluster based on 1000 bootstrap resamplings.

Deconvolution of bulk RNA-seq

Cell-type proportions in heart tissue and iPSC-CM bulk RNA-seq samples were estimated using *CIBERSORTx* [107]. Single-cell RNA-seq data from prenatal hearts (Cui *et al.* single-cell atlas [23]) was used as reference and converted into a signature matrix using 50 replicates per cell type and retaining only genes with an average expression > 0.5. To estimate cell-type composition, *CIBERSORTx* Fractions was applied with S-mode batch correction to account for technical variability, and statistical significance was assessed with 1000 permutations for p-value calculation.

Splicing analysis

Alternative splicing (AS) events were identified and quantified using *rMATS v4.1.2*, *MAJIQ v2.5.1*, and *vast-tools v2.5.1* [108–110], which extract reads mapping to splice junctions from BAM files and calculate Percent Spliced In (PSI) values. For *rMATS*, default parameters were used (cstat 0.0001, anchorLength 3) with the -novelSS option enabled to detect unannotated splice sites. Results were filtered to retain events with ≥10 reads supporting either inclusion or skipping in at least half of the samples across at least two groups. For *MAJIQ*, a splice graph was constructed, including all binary splicing events detected in >50% of the samples per group, with a minimum of 5 supporting reads for known junctions and 7 reads for *de novo* junctions. For *vast-tools*, PSI values were computed, including intron retention events (--p_IR). Events were retained if they had sufficient read coverage in 50% of both prenatal and postnatal groups (--min_Fr 0.5), a minimum standard deviation of 5 (min_SD 5), and met the --noVLOW criterion to exclude low-coverage events. All splicing events were further filtered to retain only those with ≤1/3 missing values in prenatal and postnatal heart samples and no missing values in iPSC-CM samples.

To assess splicing similarity between samples, Spearman pairwise correlation coefficients (ρ) were computed on logit-transformed PSI values. To determine a TPM threshold for reliable PSI estimation, splicing events were binned based on the TPM of the parent gene, and the mean PSI variance of each bin was plotted. A loess smooth curve was fitted to identify the stabilization point, determining TPM > 10 as optimal for robust splicing estimation. All splicing events detected by rMATS in genes with TPM > 10 were considered, except for constitutive events where all samples exhibited a PSI of 0 or 1. The correlation matrix was generated and visualized using *corrplot v0.94* [102]. PCA was performed using PSI values from the 500 most variable splicing events and visualized using *ggplot2 v3.5.1* [105].

Significant splicing changes between groups were defined as those events with deltaPSI > +/- 0.2 and < 1% FDR for *rMATS*. With *MAJIQ* heterogen and modulize, we considered as significant binary events with a deltaPSI > +/- 0.2 and a probability of changing > 0.9. *Vast-tools* was also used to detect differentially spliced events with > 90% probability that there is a change of at least 20%.

The heatmap to visualize the differentially spliced events was generated using *pheatmap v1.0.12* [111] and *RColorBrewer v.1.1* [112]. For this, each sample's deviation from the mean of each gene was calculated as row Z-scores, and clustering was performed using complete linkage clustering with Spearman correlation as the distance metric. Visualization of specific alternative splicing events was performed with *ggashimi v1.1.5* using the respective surrounding coordinates and the median number of supporting reads for each group [113]. The potential functional impact of the alternative splicing events was investigated using *VastDB*, by matching the event coordinates with those present in the database [110]. Unless specified otherwise, all other plots were generated using the *ggplot2 v3.5.1* package [105]. When multiple transcript isoforms corresponded to a specific spliced exon/intron, we reported the isoform with the highest confidence (i.e., MANE Select transcript, ENSEMBL golden isoform, or similar high-confidence annotations), based on the GENCODE v45 human primary transcript annotation used throughout the analysis [99].

NEASE Analysis

NEASE (Network-based Enrichment Analysis for Splicing Events) *v1.2.2* was used to infer the functional impact of the identified AS events at the protein interaction network level [114]. Exons predicted to disrupt the open reading frame (ORF) were excluded from the analysis. First, we detected protein features potentially impacted by splicing, including protein domains, linear motifs and interacting residues. Then, pathways affected by interactions mediated by the spliced features were identified. One-sided hypergeometric test was performed to identify enriched pathways, applying a p-value cutoff of 0.05. Pathways were ranked based on the NEASE score.

Acknowledgements

We are grateful to Leslie Leinwand (University of Colorado, Boulder, CO, USA) and Lars Steinmetz (Stanford University, Palo Alto, CA, USA) for insightful discussions. We also thank the GIMM Flow Cytometry, Bioimaging and Genomics Facilities (Lisboa, Portugal), the BIH/MDC Genomics Technology Platform (Berlin, Germany), and Carmen Judis (MDC, Berlin, Germany) for technical support.

Funding

This work was supported by "la Caixa" Foundation under the agreement LCF/PR/HR20/52400021, and Leducq Foundation for Cardiovascular Research network research grant 21CVD02. Further support was received from Fundação para a Ciência e a Tecnologia (FCT), Portugal (Fellowship 2020.04836.BD to M.F.).

Author Contributions

B.G.-S., M.F. and M.C.-F designed the study. B.G.-S. performed the bioinformatics analyses. M.F., M.R., S.M., M.T.C. performed the experiments involving iPSC-CM differentiation and characterization. M.R. performed the titin gels. H.M. contributed to scRNA-sequencing. R.S. and M.G. provided expert guidance and feedback on analyses and results. B.G.-S., M.F. and M.C.-F wrote the manuscript, with feedback from all authors.

Declaration of interests

The authors M.R., S.M., M.F., M.T.C. and M.C.-F. filed an invention disclosure describing the cardiomyocyte differentiation protocol presented in this study (Methods of Cardiomyocyte Production, Patent # GB 2117642.5, December 7, 2021. United Kingdom Intellectual Property Office, UK). M.G. is an advisor for River Biomedics and collaborates with Ionis Pharmaceuticals. The remaining authors have nothing to disclose.

Figure Legends

Figure 1. Genome-wide comparison of splicing profiles in iPSC-CMs and developing hearts

A. Schematic representation of iPSC differentiation into iPSC-CMs. The iPSC cell lines and their respective sexes are indicated.

B-D. Immunofluorescence images showing the expression of (**B**) α-Actinin 1 and (**C**) α-MyBP-C, in iPSC-CMs on day 30 of differentiation. Samples were derived from the indicated iPSC lines. Nuclei are stained with DAPI. Scale bar included in each image.

D. UMAP plot of iPSC-CMs derived from iPSC-T, revealing two major subpopulations of cells corresponding to cardiomyocytes (red), and epicardial-derived cells (blue).

E. Schematic representation of the developing human heart RNA-seq dataset, with the corresponding timepoints.

F-G. Principal Component Analysis based on the (**F**) 500 most variable protein-coding genes and (**G**) 500 most variable splicing events, across iPSC-CMs (in red), prenatal hearts (in blue) and postnatal hearts (in green). Lighter shades represent younger samples, and darker shades correspond to older samples. Splicing events in (**G**) include exon skipping, intron retention, and alternative 3' and 5' splice sites detected by vast-tools.

H. Heatmap showing estimated cell type proportions in heart and iPSC-CM samples, determined using CIBERSORTx.

I. Barplot depicting the total number of differentially spliced events ($\Delta PSI \geq \pm 0.2$, adjusted p-value ≤ 0.01) in comparisons between Prenatal vs. Postnatal Heart, iPSC-CM vs. Prenatal Heart, and iPSC-CM vs. Postnatal Heart. Events above 0 (darker color) indicate higher inclusion in the first group of each comparison, while events below 0 (lighter color) indicate lower inclusion in the first group.

J. Heatmap displaying Z-score normalized Percent Spliced In (PSI) levels for all exon skipping events, comparing iPSC-CMs with prenatal hearts, iPSC-CMs with postnatal hearts, and prenatal hearts with postnatal hearts. Colors reflect inclusion levels relative to the mean of each event (red for higher inclusion, blue for lower inclusion).

Figure 2. Pre- to postnatal splicing transitions in the heart

A-B, D-F. Inclusion levels (PSI) of exons differentially included between prenatal and postnatal hearts, specifically (**A**) *MYOM1* exon 18 (*MYOM1*-202), (**B**) *MBNL1* exon 5 (*MBNL1*-211), **D**) *FN1* exon 25 (*FN1*-203), (**E**) *FERMT2* exon 11 (*FERMT2*-215) and (**F**) *IMMT* exon 6 (*IMMT*-204).

C. Top 5 enriched Reactome pathways identified by NEASE for differentially spliced exons identified between prenatal and postnatal hearts.

Figure 3. Heterogeneous mirroring of prenatal heart splicing regulation in iPSC-CMs

A. Heatmap displaying Z-score normalized Percent Spliced In (PSI) levels of all exon skipping events identified when comparing 4-5 weeks embryonic with 18-19 weeks fetal hearts. Colors represent inclusion levels relative to the mean for each event (red indicates higher inclusion, blue indicates lower inclusion).

B. Top 5 enriched Reactome pathways identified by NEASE for differentially spliced exons identified between 4-5 weeks embryonic and 18-19 weeks fetal hearts.

C-F. Inclusion levels (PSI) of exons differentially spliced between 4-5 weeks embryonic and 18-19 weeks fetal hearts, specifically (**C**) *MYH14* exon 6 (*MYH14*-208), (**D**) *VEGFA* exon 6 (*VEGFA*-226), (**E**) *MBNL2* exon 6 (*MBNL2*-207), and (**F**) *EML1* exon 2 (*EML1*-222). PSI levels are shown for iPSC-CMs, embryonic hearts, and fetal hearts. Each event is accompanied by the corresponding sashimi plot.

Figure 4. Maturation-driven splicing changes in iPSC-CMs recapitulate developmental transitions in the human heart

A. Diagram illustrating the differentiation protocol used to generate iPSC-CMs and the experimental conditions for assessing alternative splicing during *in vitro* maturation. Conditions

include iPSC-CMs at 30 days of differentiation, 40 days of differentiation, and 40 days of differentiation with micropatterning.

B. Immunofluorescence image showing α-Actinin 1 expression in sarcomeres of iPSC-CMs at day 30 of differentiation. Sarcomere length measurements of iPSC-CMs derived from three cell lines (T, D, C) across three experimental conditions. The number of cells quantified in each group is indicated.

C-G. Inclusion levels (PSI) of exons differentially spliced between prenatal and postnatal hearts, specifically (**C**) *TNNT2* exon 5 (*TNNT2*-224), (**D**) *CMYA5* exon 5 (*CMYA5*-201), (**E**) *LDB3* exon 8 (*LDB3*-202), (**F**) *TRDN* exon 19 (*TRDN*-201) and (**G**) *CAMK2D* exon 18 (*CAMK2D*-202). PSI levels are shown for iPSC-CMs, prenatal hearts, and postnatal hearts across various developmental time points. Each splicing event is accompanied by *in vitro* PCR quantification performed in three distinct cell lines (T, D and C) under three experimental conditions: 30 days of differentiation (in red), 40 days of differentiation (in pink), and 40 days of differentiation with micropatterning (in dark red).

Figure 5. A subset of splicing events distinguishes iPSC-CMs from hearts

A. Top 5 enriched Reactome pathways identified by NEASE for differentially spliced exons identified between iPSC-CMs and both prenatal and postnatal hearts.

B-G. Inclusion levels (PSI) of exons/introns differentially spliced between iPSC-CMs and both prenatal and postnatal hearts, specifically (**B**) *CLK1* exon 4 (*CLK1*-201), (**C**) *CLK4* exon 4 (*CLK4*-201), (**D**) *SNRPE* exon 2 (*SNRPE*-202), (**E**) *RSRP1* exon 4 (*RSRP1-204)*, (**F**) *UPF3A* exon 4 (*UPF3A*-202), and (**G**) *METTL3* intron 8 (*METTL3*-201). PSI levels are shown for iPSC-CMs, prenatal hearts, and postnatal hearts. (**B**), (**C**), (**D**) and (**G**) are accompanied by *in vitro* PCR quantification performed in three distinct cell lines (T, D and C) under four experimental conditions: iPSC not differentiated (in grey), 30 days of differentiation (in red), 40 days of differentiation (in pink), and 40 days of differentiation with micropatterning (in dark red).

Supplementary Figure 1. Genome-wide comparison of splicing profiles in iPSC-CMs and developing hearts

A. UMAP plot of iPSC-CMs derived from iPSC-D, revealing two major subpopulations of cells corresponding to cardiomyocytes (red), and epicardial-derived cells (blue).

B. Dot plot of the expression of markers for the cell types identified in (**A**). Dot size represents the percentage of cells expressing each gene, and dot color indicates scaled expression levels averaged per cell population.

C. UMAP plots displaying the enriched expression of mitochondrial genes in iPSC-CM derived from iPSC-T.

D. UMAP plot of iPSC-CMs derived from iPSC-T with cell type annotations based on label transfer from the *Cui et al.* single-cell atlas.

E. Gene set enrichment analysis of population-specific markers with adjusted p-value <= 0.01 sorted by average log2FC.

F. Correlation matrix showing gene expression similarities (TPM > 1) between iPSC-CM cultures derived from iPSC-D, iPSC-G, and iPSC-T, and two distinct 4-week embryonic hearts. Gene expression counts were rlog-transformed, and pairwise correlation coefficients were computed using Pearson correlation.

G. Venn diagram illustrating the overlap of the protein-coding genes expressed (TPM>1) in iPSC-CM cultures derived from iPSC-D (green), iPSC-G (orange) and iPSC-T (purple).

H. Unsupervised hierarchical clustering of all samples, based on 1 – pairwise Spearman correlation coefficients, utilizing the average linkage method. Samples are colored according to their group (iPSC-CMs - red; prenatal heart – blue; postnatal heart - green).

I. Scatterplots comparing the inclusion levels (TPM>10) of all alternative splicing events detected by rMATS in iPSC-CM cultures derived from iPSC-D, iPSC-G and iPSC-T. Constitutive events with a Percent Spliced In (PSI) of 0 or 1 were removed. PSIs were logit-transformed and pairwise correlation coefficients were calculated using Spearman correlation.

J-K. PCA of the 500 most variable splicing events in iPSC-CMs (red), prenatal hearts (in blue) and postnatal hearts (in green), as identified by (**F**) MAJIQ and (**G**) rMATS. Lighter colors represent younger samples, while darker colors represent older samples.

M. PCA of the 500 most variable splicing events detected by vast-tools, colored by the proportion of cardiomyocytes (estimated by CIBERSORTx) in iPSC-CM, prenatal heart, and postnatal heart samples.

N. Heatmap displaying Z-score normalized Percent Spliced In (PSI) levels for all intron retention events, comparing iPSC-CMs with prenatal hearts, iPSC-CMs with postnatal hearts, and prenatal hearts with postnatal hearts. Colors reflect inclusion relative to the mean of each event (red for higher inclusion, blue for lower inclusion).

Supplementary Figure 2. Pre- to postnatal splicing transitions in the heart

A. Western blot displaying the resolution of TTN isoforms in iPSC-CMs derived from iPSC-T and iPSC-D. Human left ventricle is used as control.

B-K. Inclusion levels (PSI) of exons differentially included between prenatal and postnatal hearts, specifically (**B**) *FN1* exon 33 (*FN1*-203), (**C**) *FBLN2* exon 9 (*FBLN2*-203), (**D**) *TNNT2* exon 10 (*TNNT2*-203), (**E**) *TPM3* exon 5 (*TPM3*-211), (**F**) *ACTN4* exon 8 (*ACTN4*-201), (**G**) *MYL6* exon 6 (*MYL6*-218), (**H**) *MEF2D* exon 8 (*MEF2D*-201), (**I**) *TCF3* exon 18 (*TCF3*-203), (**J**) *MLF1* exon 3 (*MLF1*-203), (**K**) *PKM* exon 9 (*PKM*-219). PSI levels are shown for iPSC-CMs, prenatal hearts, and postnatal hearts across various developmental time points. Each event is accompanied by the corresponding sashimi plot.

Supplementary Figure 3. Heterogeneous mirroring of prenatal heart splicing regulation in iPSC-CMs

A. PCA of the 500 most variable splicing events in iPSC-CMs (red), 4-5 weeks embryonic hearts (in light blue) and 18-19 weeks fetal hearts (in dark blue), as identified by MAJIQ.

B. Heatmap displaying Z-score normalized Percent Spliced In (PSI) levels of all intron retention found when comparing 4-5 weeks embryonic with 18-19 weeks fetal hearts. Colors represent inclusion levels relative to the mean for each event (red indicates higher inclusion, blue indicates lower inclusion).

C-K. Inclusion levels (PSI) of exons differentially spliced between 4-5 weeks embryonic and 18-19 weeks fetal hearts, specifically (**C**) *MYO18A* exon 11 (*MYO18A*-203), (**D**) *LAMA2* exon 53 (*LAMA2*-201), (**E**) *ANK3* exon 16 (*ANK3*-201), (**F**) *ABI1* exon 4 (*ABI1*-206), (**G**) *DCAF6* exon 17 (*DCAF6*-202), (**H**) *SLC25A3* exon 3 (*SLC25A3*-202), (**I**) *ATP2B4* exon 7 (*ATP2B4*-203), (**J**) *MYO5A* exon 8 (*MYO5A*-202). PSI levels are shown for iPSC-CMs, embryonic hearts, and fetal hearts. Each event in accompanied the corresponding sashimi plot.

Supplementary Figure 4. Maturation-driven splicing changes in iPSC-CMs recapitulate developmental transitions in the human heart

A, C-E. Inclusion levels (PSI) of exons/introns differentially spliced between prenatal and postnatal hearts, specifically (**A**) *CMYA5* intron 8 (*CMYA5*-201), (**C**) *LDB3* exon 5 (*LDB3*-202), (**D**) *LDB3* exon 5 (*LDB3*-205) and (**E**) *LDB3* exon 6 (*LDB3*-205). PSI levels are shown for iPSC-CMs, prenatal hearts, and postnatal hearts across various developmental time points.

B. Correlation between the Percent Spliced In of *CMYA5* exon 5, which is predicted to lead to NMD when spliced out, and *CMYA5* gene expression levels.

Supplementary Figure 5. A subset of splicing events distinguishes iPSC-CMs from hearts

A, C-H. Inclusion levels (PSI) of exons/introns differentially spliced between iPSC-CMs and both prenatal and postnatal hearts, specifically (**A**) *TPM1* exon 2 (*TPM1*-207), (**C**) *SRSF3* intron 3 (*SRSF3*-202), (**D**) *SRSF6* intron 2 (*SRSF6*-201), (**E**) *TRA2B* intron 1 (*TRA2B*-204), (**F**) *SRSF1* intron 3 (*SRSF1*-201), (**G**) *SRSF5* intron 5 (*SRSF5*-201), (**H**) *PATL1* exon 7 (*PATL1*-201). PSI levels are shown for iPSC-CMs, prenatal hearts, and postnatal hearts.

B. Correlation between the Percent Spliced In of *RSRP1* exon 4, which is predicted to lead to NMD when included, and *RSRP1* gene expression levels.

Supplemental Information

Document S1. Figures S1-S5

Table S1. Sequencing metrics of single-cell and bulk RNA-sequencing from iPSC-CMs.

Table S2. Differentially spliced events detected between prenatal and postnatal human hearts.

Table S3. Differentially spliced events detected between iPSC-CMs and prenatal hearts, and between iPSC-CMs and postnatal hearts.

Table S4. Selected AS events between prenatal and postnatal human hearts, along with their predicted functional impact.

Table S5. Differentially spliced events detected between embryonic and fetal hearts.

Table S6. Selected AS events between embryonic and fetal human hearts, along with their functional impact.

Table S7. Differentially spliced detected iPSC-CM-specific events.

Table S8. Selected iPSC-CM-specific AS events, along with their predicted functional impact.

Table S9. RBPs differentially expressed between iPSC-CMs and both prenatal and postnatal hearts.

Table S10. Primers used for alternative splicing events.

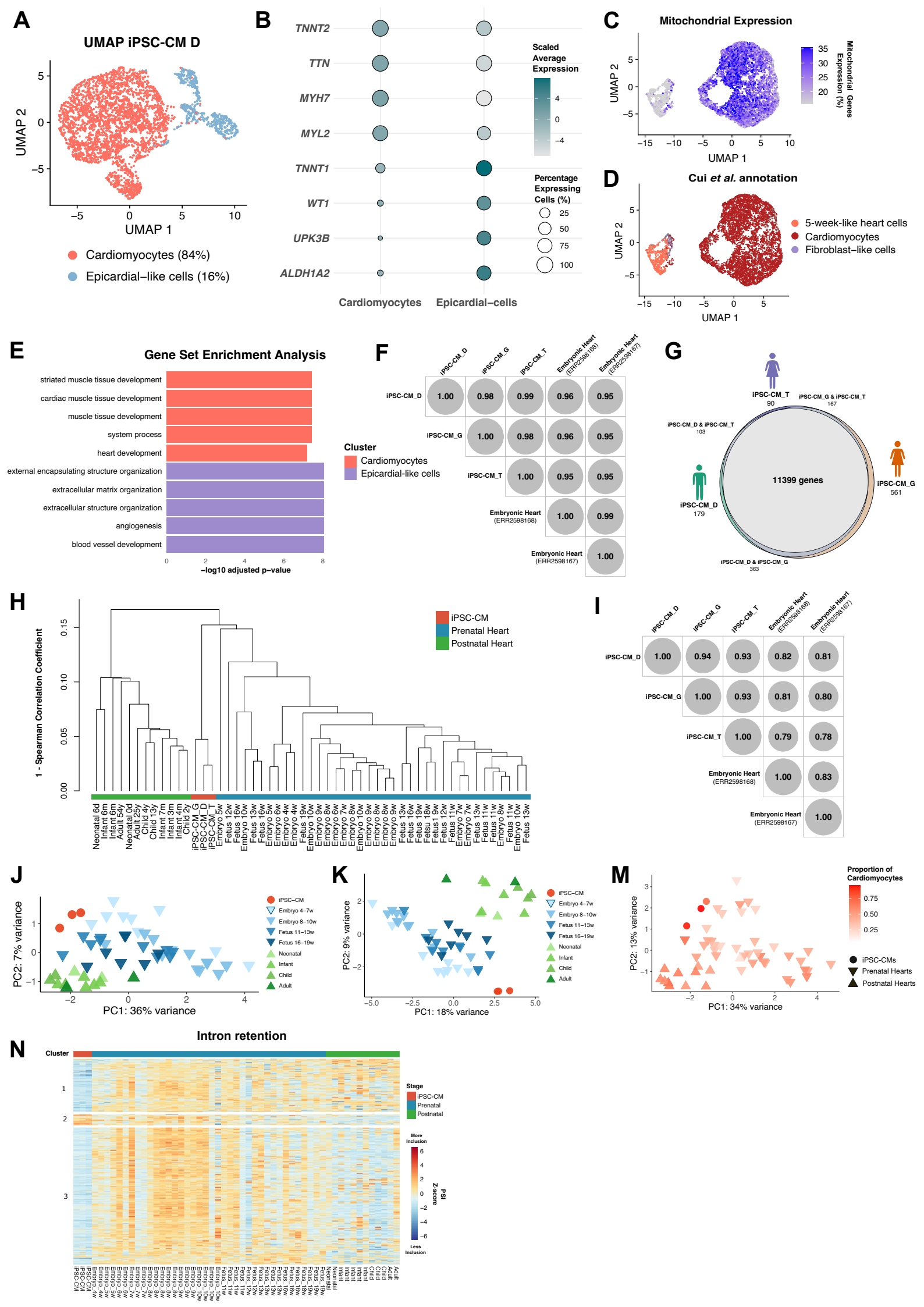
A
UMAP iPSC-CM D
UMAP 2
UMAP 1
Cardiomyocytes (84%)
Epicardial–like cells (16%)
B
TNNT2
TTN
MYH7
MYL2
TNNT1
WT1
UPK3B
ALDH1A2
Cardiomyocytes
Epicardial–cells
Scaled Average Expression
Percentage Expressing Cells (%)
C
Mitochondrial Expression
Mitochondrial Genes Expression (%)
D
Cui et al. annotation
5-week-like heart cells
Cardiomyocytes
Fibroblast–like cells
E
Gene Set Enrichment Analysis
striated muscle tissue development
cardiac muscle tissue development
muscle tissue development
system process
heart development
external encapsulating structure organization
extracellular matrix organization
extracellular structure organization
angiogenesis
blood vessel development
−log10 adjusted p−value
F
iPSC-CM_D
iPSC-CM_G
iPSC-CM_T
Embryonic Heart (ERR2598168)
Embryonic Heart (ERR2598167)
Cluster
Cardiomyocytes
Epicardial-like cells
G
iPSC-CM_T 90
iPSC-CM_G & iPSC-CM_T 167
iPSC-CM_D & iPSC-CM_T 103
11399 genes
iPSC-CM_G 561
iPSC-CM_D 179
iPSC-CM_D & iPSC-CM_G 363
H
1 - Spearman Correlation Coefficient
iPSC-CM
Prenatal Heart
Postnatal Heart
I
J
PC2: 7% variance
PC1: 36% variance
iPSC−CM
Embryo 4−7w
Embryo 8−10w
Fetus 11−13w
Fetus 16−19w
Neonatal
Infant
Child
Adult
K
PC2: 9% variance
PC1: 18% variance
M
Proportion of Cardiomyocytes
PC2: 13% variance
PC1: 34% variance
iPSC-CMs
Prenatal Hearts
Postnatal Hearts
N
Intron retention
Cluster
Stage
iPSC-CM
Prenatal
Postnatal
More Inclusion
Less Inclusion
PSI Z-score

Figure S1. Genome-wide comparison of splicing profiles in iPSC-CMs and developing hearts

A. UMAP plot of iPSC-CMs derived from iPSC-D, revealing two major subpopulations of cells corresponding to cardiomyocytes (red), and epicardial-derived cells (blue).
B. Dot plot of the expression of markers for the cell types identified in **(A**). Dot size represents the percentage of cells expressing each gene, and dot color indicates scaled expression levels averaged per cell population.
C. UMAP plots displaying the enriched expression of mitochondrial genes in iPSC-CM derived from iPSC-T.
D. UMAP plot of iPSC-CMs derived from iPSC-T with cell type annotations based on label transfer from the Cui et al. single-cell atlas.
E. Gene set enrichment analysis of population-specific markers with adjusted p-value <= 0.01 sorted by average log2FC.
F. Correlation matrix showing gene expression similarities (TPM > 1) between iPSC-CM cultures derived from iPSC-D, iPSC-G, and iPSC-T, and two distinct 4-week embryonic hearts. Gene expression counts were rlog-transformed, and pairwise correlation coefficients were computed using Pearson correlation.
G. Venn diagram illustrating the overlap of the protein-coding genes expressed (TPM>1) in iPSC-CM cultures derived from iPSC-D (green), iPSC-G (orange) and iPSC-T (purple).
H. Unsupervised hierarchical clustering of all samples, based on 1 – pairwise Spearman correlation coefficients, utilizing the average linkage method. Samples are colored according to their group (iPSC-CMs - red; prenatal heart – blue; postnatal heart - green).
I. Scatterplots comparing the inclusion levels (TPM>10) of all alternative splicing events detected by rMATS in iPSC-CM cultures derived from iPSC-D, iPSC-G and iPSC-T. Constitutive events with a Percent Spliced In (PSI) of 0 or 1 were removed. PSIs were logit-transformed and pairwise correlation coefficients were calculated using Spearman correlation.
J-K. PCA of the 500 most variable splicing events in iPSC-CMs (red), prenatal hearts (in blue) and postnatal hearts (in green), as identified by (**F**) MAJIQ and (**G**) rMATS. Lighter colors represent younger samples, while darker colors represent older samples.
M. PCA of the 500 most variable splicing events detected by vast-tools, colored by the proportion of cardiomyocytes (estimated by CIBERSORTx) in iPSC-CM, prenatal heart, and postnatal heart samples.
N. Heatmap displaying Z-score normalized Percent Spliced In (PSI) levels for all intron retention events, comparing iPSC-CMs with prenatal hearts, iPSC-CMs with postnatal hearts, and prenatal hearts with postnatal hearts. Colors reflect inclusion relative to the mean of each event (red for higher inclusion, blue for lower inclusion).

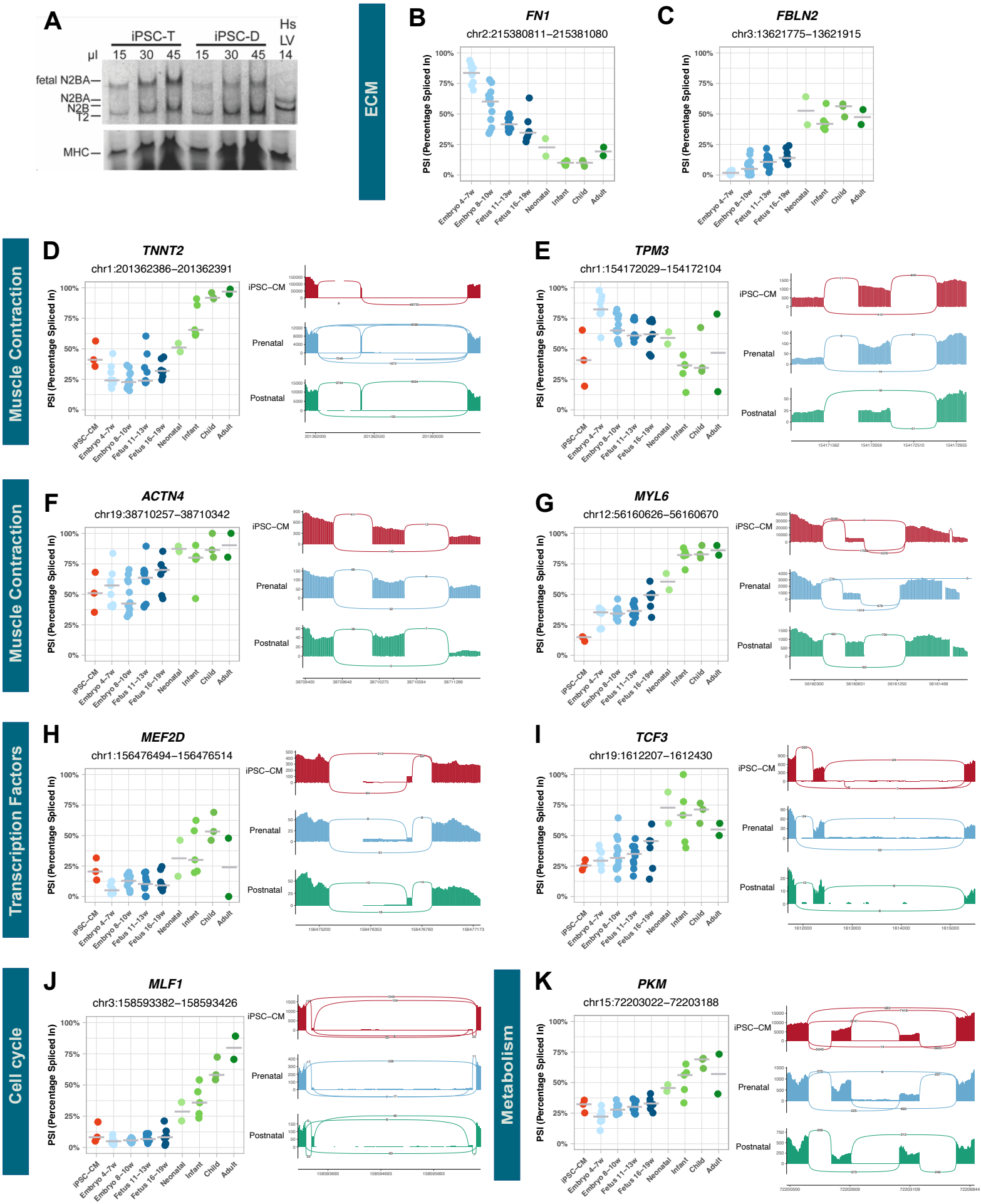

Figure S2. Pre- to postnatal splicing transitions in the heart

A. Western blot displaying the resolution of TTN isoforms in iPSC-CMs derived from iPSC-T and iPSC-D. Human left ventricle is used as control.

B-K. Inclusion levels (PSI) of exons differentially included between prenatal and postnatal hearts, specifically (**B**) *FN1* exon 33 (*FN1*-203), (**C**) *FBLN2* exon 9 (*FBLN2*-203), (**D**) *TNNT2* exon 10 (*TNNT2*-203), (**E**) *TPM3* exon 5 (*TPM3*-211), (**F**) *ACTN4* exon 8 (*ACTN4*-201), (**G**) *MYL6* exon 6 (*MYL6*-218), (**H**) *MEF2D* exon 8 (*MEF2D*-201), (**I**) *TCF3* exon 18 (*TCF3*-203), (**J**) *MLF1* exon 3 (*MLF1*-203), (**K**) *PKM* exon 9 (*PKM*-219). PSI levels are shown for iPSC-CMs, prenatal hearts, and postnatal hearts across various developmental time points. Each event is accompanied by the corresponding sashimi plot.

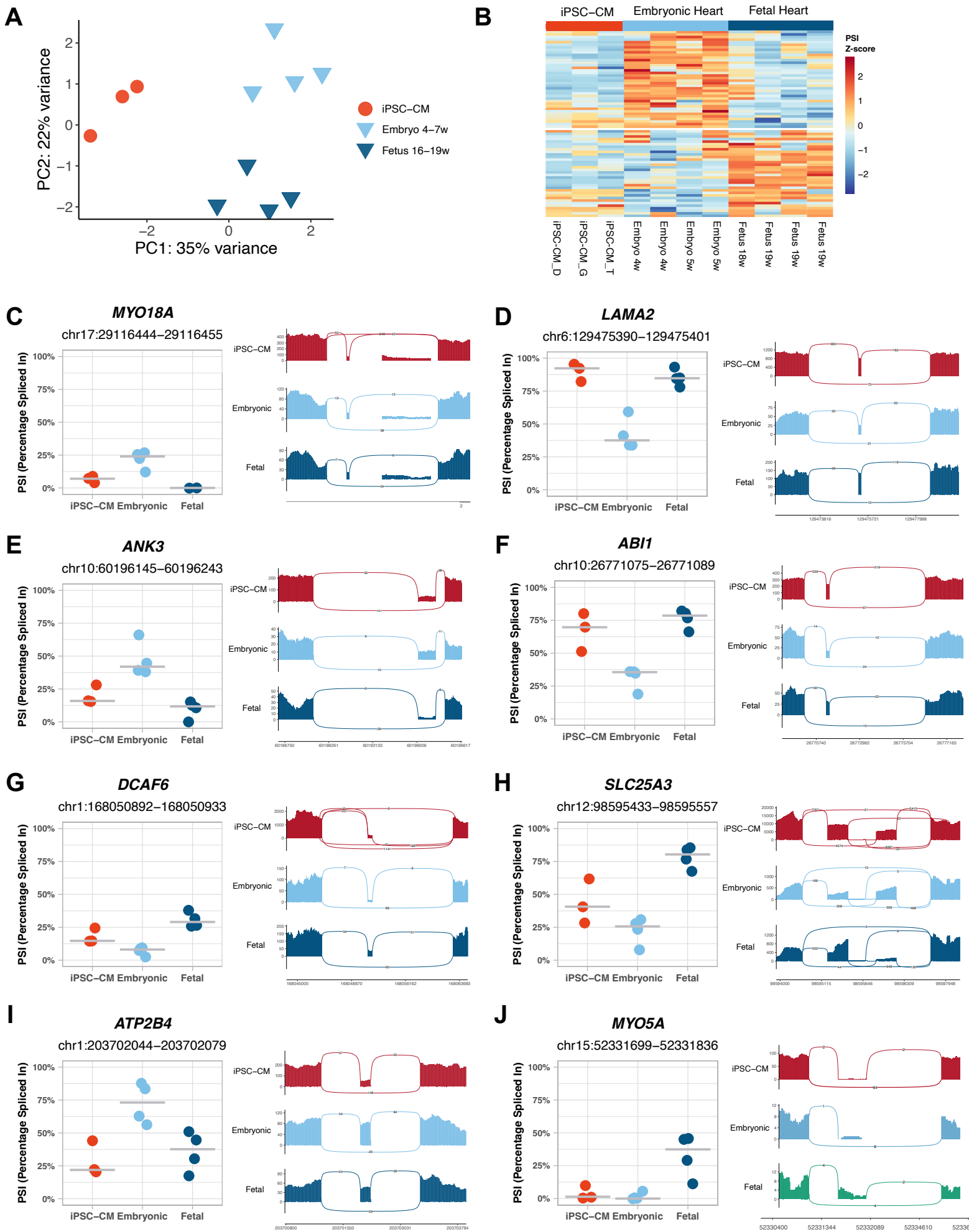
A
PC2: 22% variance
PC1: 35% variance
iPSC−CM
Embryo 4−7w
Fetus 16−19w
B
iPSC−CM
Embryonic Heart
Fetal Heart
PSI Z-score
iPSC-CM_D
iPSC-CM_G
iPSC-CM_T
Embryo 4w
Embryo 4w
Embryo 5w
Embryo 5w
Fetus 18w
Fetus 19w
Fetus 19w
Fetus 19w
C
MYO18A
chr17:29116444−29116455
D
LAMA2
chr6:129475390−129475401
E
ANK3
chr10:60196145−60196243
F
ABI1
chr10:26771075−26771089
G
DCAF6
chr1:168050892−168050933
H
SLC25A3
chr12:98595433−98595557
I
ATP2B4
chr1:203702044−203702079
J
MYO5A
chr15:52331699−52331836
PSI (Percentage Spliced In)
iPSC−CM
Embryonic
Fetal

Supplementary Figure 3. Heterogeneous mirroring of prenatal heart splicing regulation in iPSC-CMs

A. PCA of the 500 most variable splicing events in iPSC-CMs (red), 4-5 weeks embryonic hearts (in light blue) and 18-19 weeks fetal hearts (in dark blue), as identified by MAJIQ.
B. Heatmap displaying Z-score normalized Percent Spliced In (PSI) levels of all intron retention found when comparing 4-5 weeks embryonic with 18-19 weeks fetal hearts. Colors represent inclusion levels relative to the mean for each event (red indicates higher inclusion, blue indicates lower inclusion).
C-K. Inclusion levels (PSI) of exons differentially spliced between 4-5 weeks embryonic and 18-19 weeks fetal hearts, specifically (**C**) *MYO18A* exon 11 (*MYO18A*-203), (**D**) *LAMA2* exon 53 (*LAMA2*-201), (**E**) *ANK3* exon 16 (*ANK3*-201), (**F**) *ABI1* exon 4 (*ABI1*-206), (**G**) *DCAF6* exon 17 (*DCAF6*-202), (**H**) *SLC25A3* exon 3 (*SLC25A3*-202), (**I**) *ATP2B4* exon 7 (*ATP2B4*-203), (**J**) *MYO5A* exon 8 (*MYO5A*-202). PSI levels are shown for iPSC-CMs, embryonic hearts, and fetal hearts. Each event in accompanied the corresponding sashimi plot.

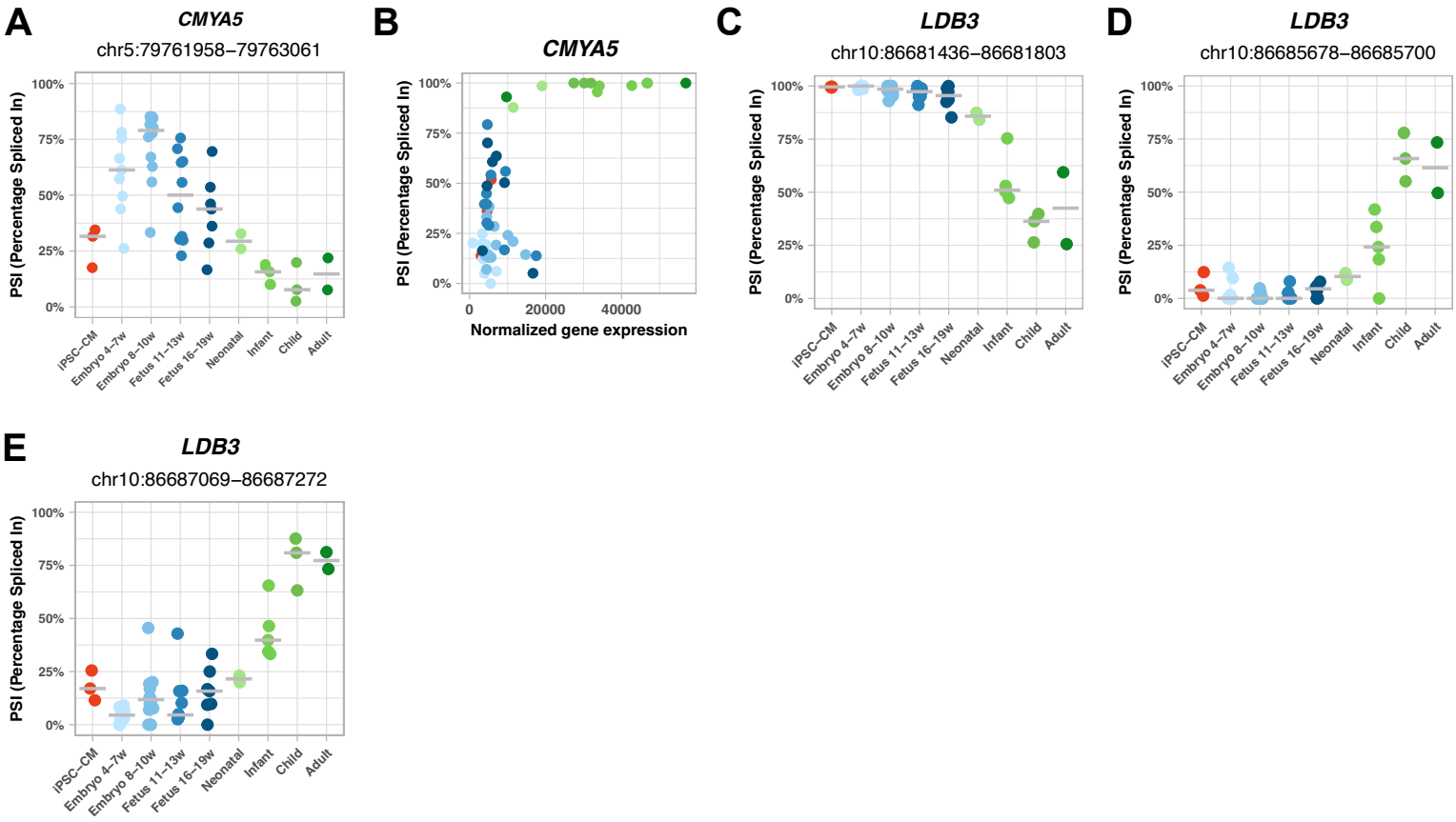

Figure S4. Maturation-driven splicing changes in iPSC-CMs recapitulate developmental transitions in the human heart

A, C-E. Inclusion levels (PSI) of exons/introns differentially spliced between prenatal and postnatal hearts, specifically (**A**) *CMYA5* intron 8 (*CMYA5*-201), (**C**) *LDB3* exon 5 (*LDB3*-202), (**D**) *LDB3* exon 5 (*LDB3*-205) and (**E**) *LDB3* exon 6 (*LDB3*-205). PSI levels are shown for iPSC-CMs, prenatal hearts, and postnatal hearts across various developmental time points.
B. Correlation between the Percent Spliced In of *CMYA5* exon 5, which is predicted to lead to NMD when spliced out, and *CMYA5* gene expression levels.

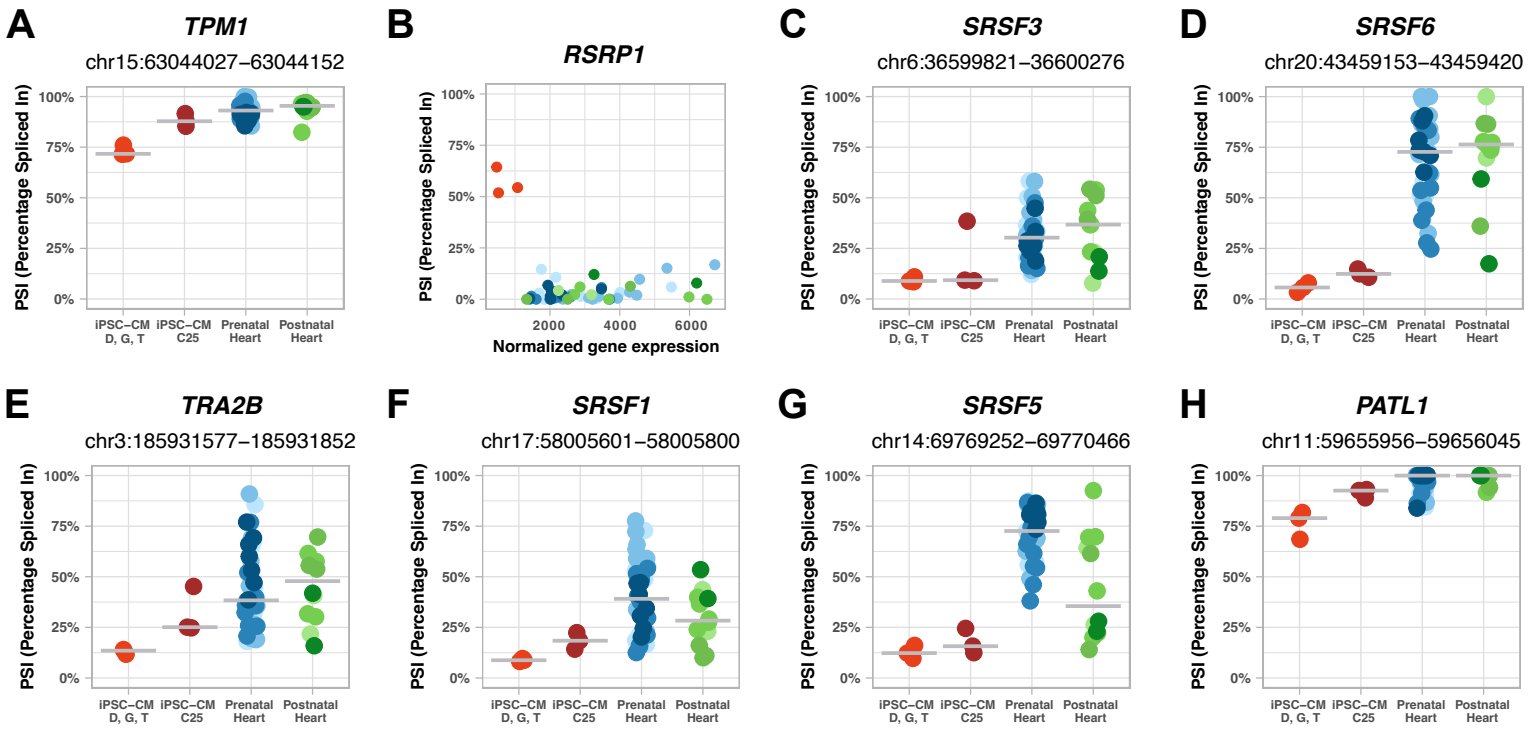

Figure S5. A subset of splicing events distinguishes iPSC-CMs from hearts

A, C-H. Inclusion levels (PSI) of exons/introns differentially spliced between iPSC-CMs and both prenatal and postnatal hearts, specifically (**A**) *TPM1* exon 2 (*TPM1*-207), (**C**) *SRSF3* intron 3 (*SRSF3*-202), (**D**) *SRSF6* intron 2 (*SRSF6*-201), (**E**) *TRA2B* intron 1 (*TRA2B*-204), (**F**) *SRSF1* intron 3 (*SRSF1*-201), (**G**) *SRSF5* intron 5 (*SRSF5*-201), (**H**) *PATL1* exon 7 (*PATL1*-201). PSI levels are shown for iPSC-CMs, prenatal hearts, and postnatal hearts.
B. Correlation between the Percent Spliced In of *RSRP1* exon 4, which is predicted to lead to NMD when included, and *RSRP1* gene expression levels.

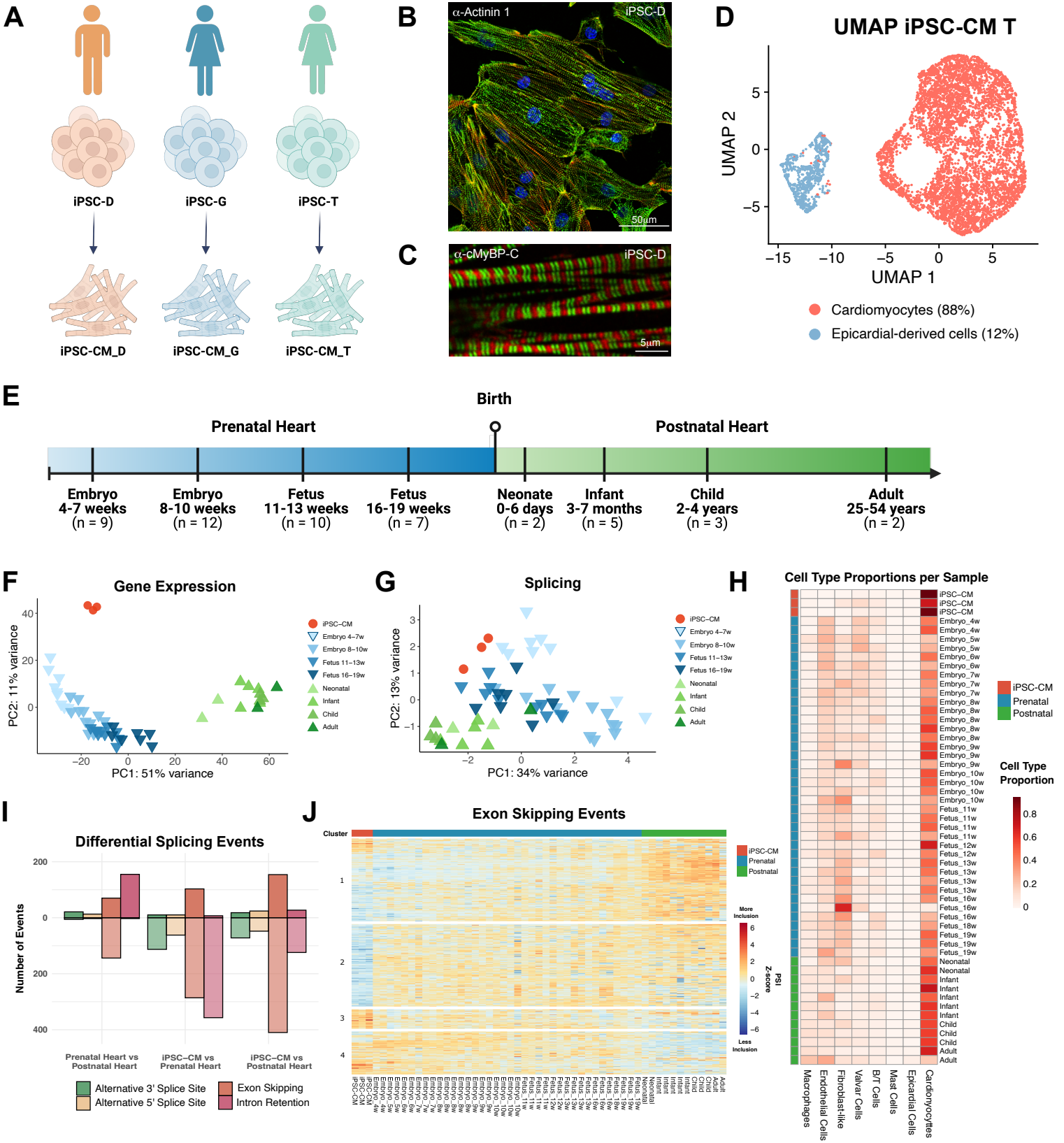
A
iPSC-D
iPSC-G
iPSC-T
iPSC-CM_D
iPSC-CM_G
iPSC-CM_T
B
α-Actinin 1
iPSC-D
50μm
C
α-cMyBP-C
iPSC-D
5μm
D
UMAP iPSC-CM T
UMAP 2
UMAP 1
Cardiomyocytes (88%)
Epicardial-derived cells (12%)
E
Birth
Prenatal Heart
Postnatal Heart
Embryo 4-7 weeks (n = 9)
Embryo 8-10 weeks (n = 12)
Fetus 11-13 weeks (n = 10)
Fetus 16-19 weeks (n = 7)
Neonate 0-6 days (n = 2)
Infant 3-7 months (n = 5)
Child 2-4 years (n = 3)
Adult 25-54 years (n = 2)
F
Gene Expression
PC2: 11% variance
PC1: 51% variance
iPSC–CM
Embryo 4–7w
Embryo 8–10w
Fetus 11–13w
Fetus 16–19w
Neonatal
Infant
Child
Adult
G
Splicing
PC2: 13% variance
PC1: 34% variance
H
Cell Type Proportions per Sample
iPSC-CM
Prenatal
Postnatal
Cell Type Proportion
Macrophages
Endothelial Cells
Fibroblast-like
Valvar Cells
B/T Cells
Mast Cells
Epicardial Cells
Cardiomyocytes
I
Differential Splicing Events
Number of Events
Prenatal Heart vs Postnatal Heart
iPSC–CM vs Prenatal Heart
iPSC–CM vs Postnatal Heart
Alternative 3' Splice Site
Alternative 5' Splice Site
Exon Skipping
Intron Retention
J
Exon Skipping Events
Cluster
More Inclusion
Less Inclusion
PSI Z-score

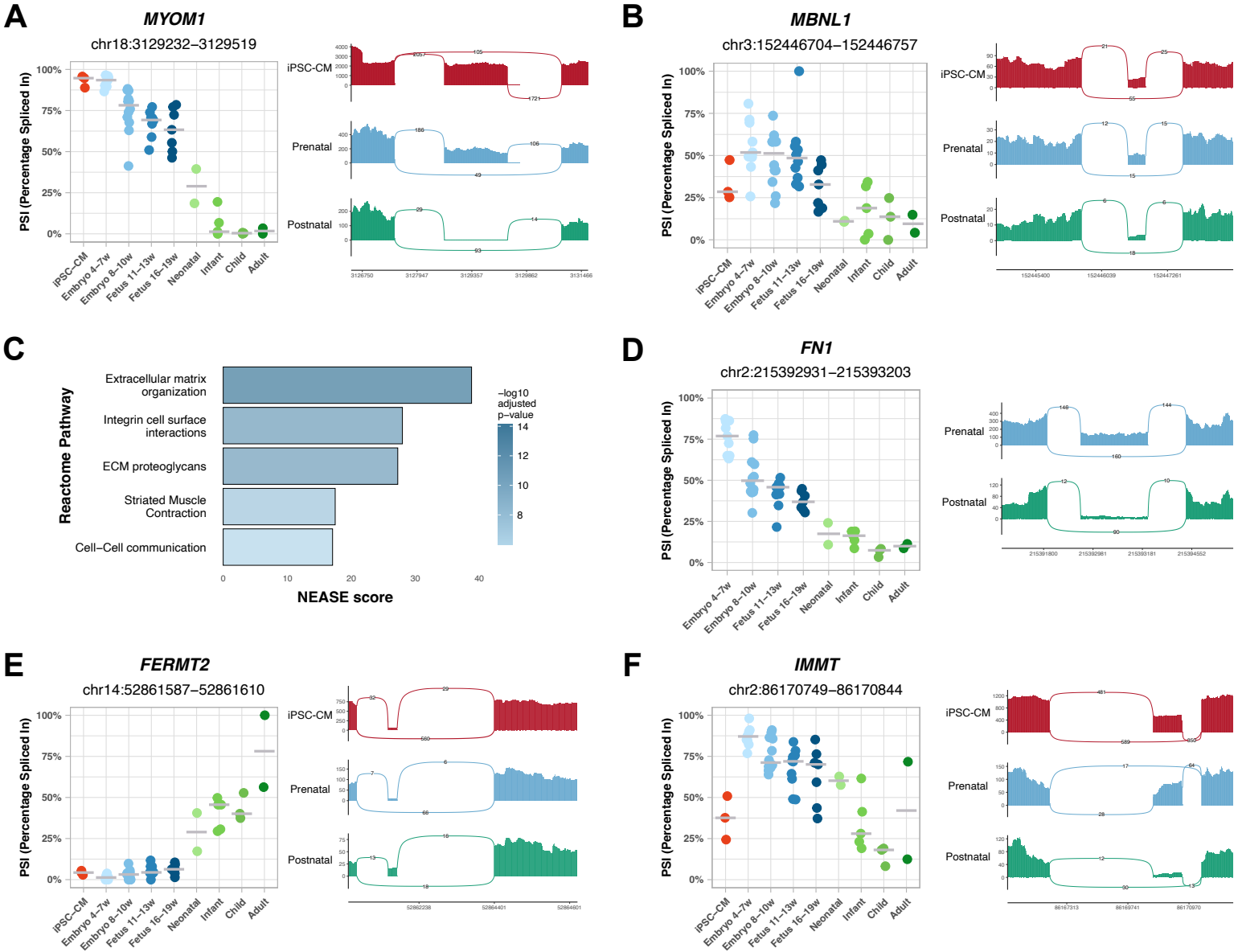
A
MYOM1
chr18:3129232–3129519
PSI (Percentage Spliced In)
100%
75%
50%
25%
0%
iPSC-CM
Embryo 4–7w
Embryo 8–10w
Fetus 11–13w
Fetus 16–19w
Neonatal
Infant
Child
Adult
iPSC-CM
Prenatal
Postnatal
B
MBNL1
chr3:152446704–152446757
C
Reactome Pathway
Extracellular matrix organization
Integrin cell surface interactions
ECM proteoglycans
Striated Muscle Contraction
Cell–Cell communication
NEASE score
−log10 adjusted p−value
D
FN1
chr2:215392931–215393203
E
FERMT2
chr14:52861587–52861610
F
IMMT
chr2:86170749–86170844

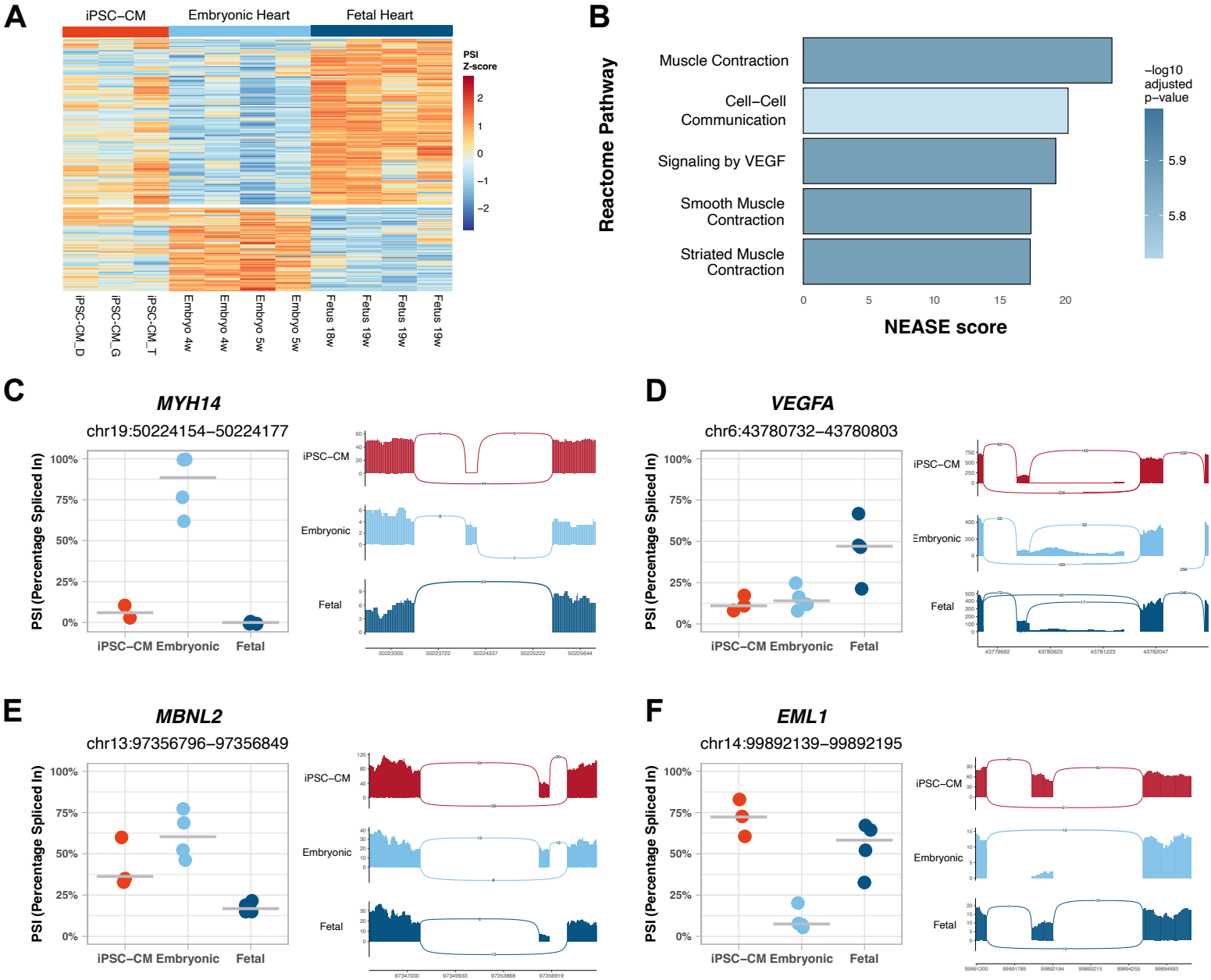
A
iPSC–CM
Embryonic Heart
Fetal Heart
PSI Z-score
2
1
0
−1
−2
iPSC-CM_D
iPSC-CM_G
iPSC-CM_T
Embryo 4w
Embryo 4w
Embryo 5w
Embryo 5w
Fetus 18w
Fetus 19w
Fetus 19w
Fetus 19w
B
Reactome Pathway
Muscle Contraction
Cell–Cell Communication
Signaling by VEGF
Smooth Muscle Contraction
Striated Muscle Contraction
0
5
10
15
20
NEASE score
−log10 adjusted p−value
5.9
5.8
C
MYH14
chr19:50224154–50224177
PSI (Percentage Spliced In)
100%
75%
50%
25%
0%
iPSC–CM Embryonic Fetal
iPSC–CM
Embryonic
Fetal
D
VEGFA
chr6:43780732–43780803
PSI (Percentage Spliced In)
100%
75%
50%
25%
0%
iPSC–CM Embryonic Fetal
iPSC–CM
Embryonic
Fetal
E
MBNL2
chr13:97356796–97356849
PSI (Percentage Spliced In)
100%
75%
50%
25%
0%
iPSC–CM Embryonic Fetal
iPSC–CM
Embryonic
Fetal
F
EML1
chr14:99892139–99892195
PSI (Percentage Spliced In)
100%
75%
50%
25%
0%
iPSC–CM Embryonic Fetal
iPSC–CM
Embryonic
Fetal

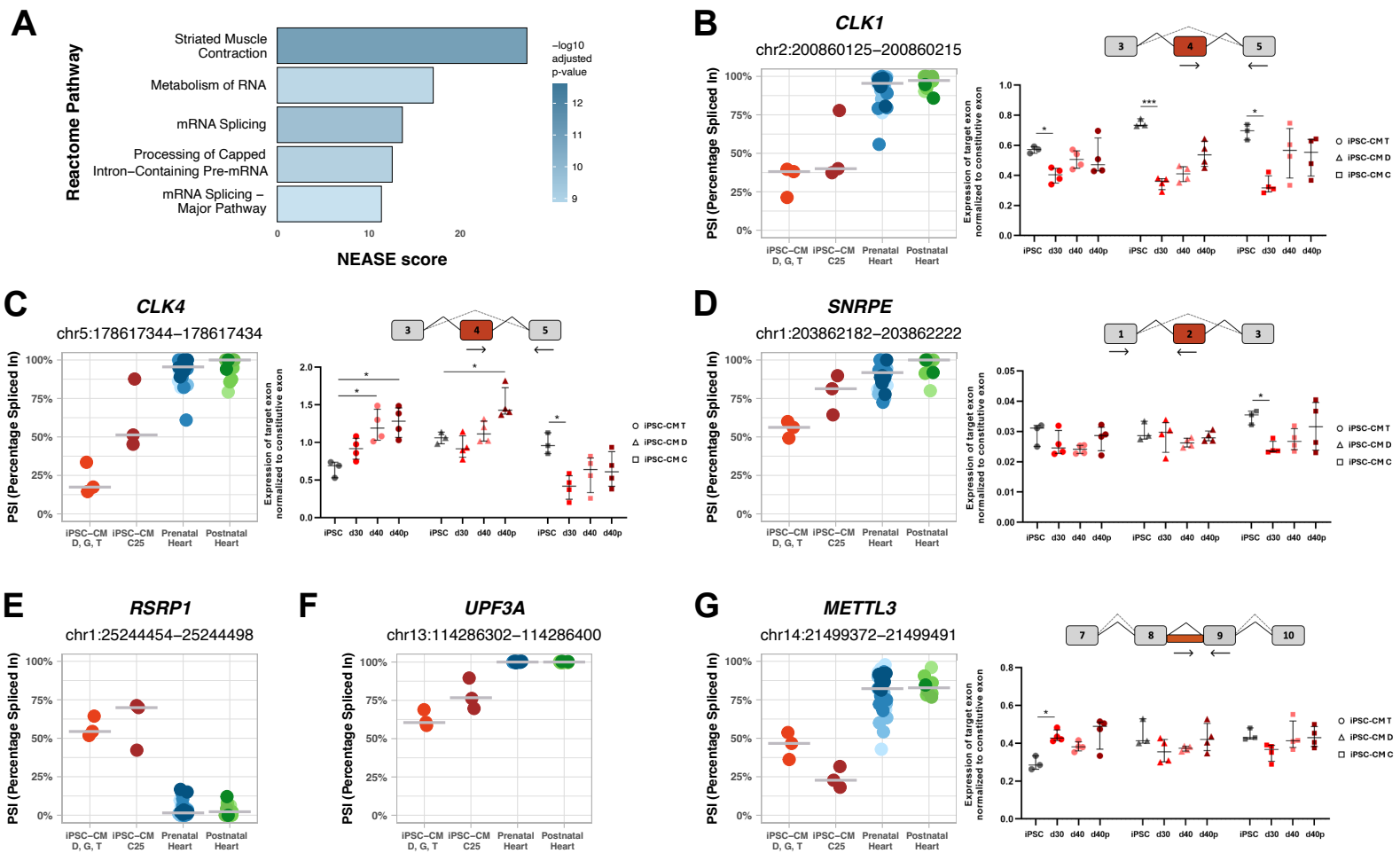
A
Reactome Pathway
Striated Muscle Contraction
Metabolism of RNA
mRNA Splicing
Processing of Capped Intron−Containing Pre-mRNA
mRNA Splicing − Major Pathway
−log10 adjusted p-value
12
11
10
9
0
10
20
NEASE score
B
CLK1
chr2:200860125−200860215
PSI (Percentage Spliced In)
100%
75%
50%
25%
0%
iPSC−CM D, G, T
iPSC−CM C25
Prenatal Heart
Postnatal Heart
3
4
5
Expression of target exon normalized to constitutive exon
1.0
0.8
0.6
0.4
0.2
0.0
*
***
*
iPSC
d30
d40
d40p
iPSC-CM T
iPSC-CM D
iPSC-CM C
C
CLK4
chr5:178617344−178617434
PSI (Percentage Spliced In)
100%
75%
50%
25%
0%
iPSC−CM D, G, T
iPSC−CM C25
Prenatal Heart
Postnatal Heart
3
4
5
Expression of target exon normalized to constitutive exon
2.0
1.5
1.0
0.5
0.0
*
*
*
*
iPSC
d30
d40
d40p
iPSC-CM T
iPSC-CM D
iPSC-CM C
D
SNRPE
chr1:203862182−203862222
PSI (Percentage Spliced In)
100%
75%
50%
25%
0%
iPSC−CM D, G, T
iPSC−CM C25
Prenatal Heart
Postnatal Heart
1
2
3
Expression of target exon normalized to constitutive exon
0.05
0.04
0.03
0.02
0.01
0.00
*
iPSC
d30
d40
d40p
iPSC-CM T
iPSC-CM D
iPSC-CM C
E
RSRP1
chr1:25244454−25244498
PSI (Percentage Spliced In)
100%
75%
50%
25%
0%
iPSC−CM D, G, T
iPSC−CM C25
Prenatal Heart
Postnatal Heart
F
UPF3A
chr13:114286302−114286400
PSI (Percentage Spliced In)
100%
75%
50%
25%
0%
iPSC−CM D, G, T
iPSC−CM C25
Prenatal Heart
Postnatal Heart
G
METTL3
chr14:21499372−21499491
PSI (Percentage Spliced In)
100%
75%
50%
25%
0%
iPSC−CM D, G, T
iPSC−CM C25
Prenatal Heart
Postnatal Heart
7
8
9
10
Expression of target exon normalized to constitutive exon
0.8
0.6
0.4
0.2
0.0
*
iPSC
d30
d40
d40p
iPSC-CM T
iPSC-CM D
iPSC-CM C

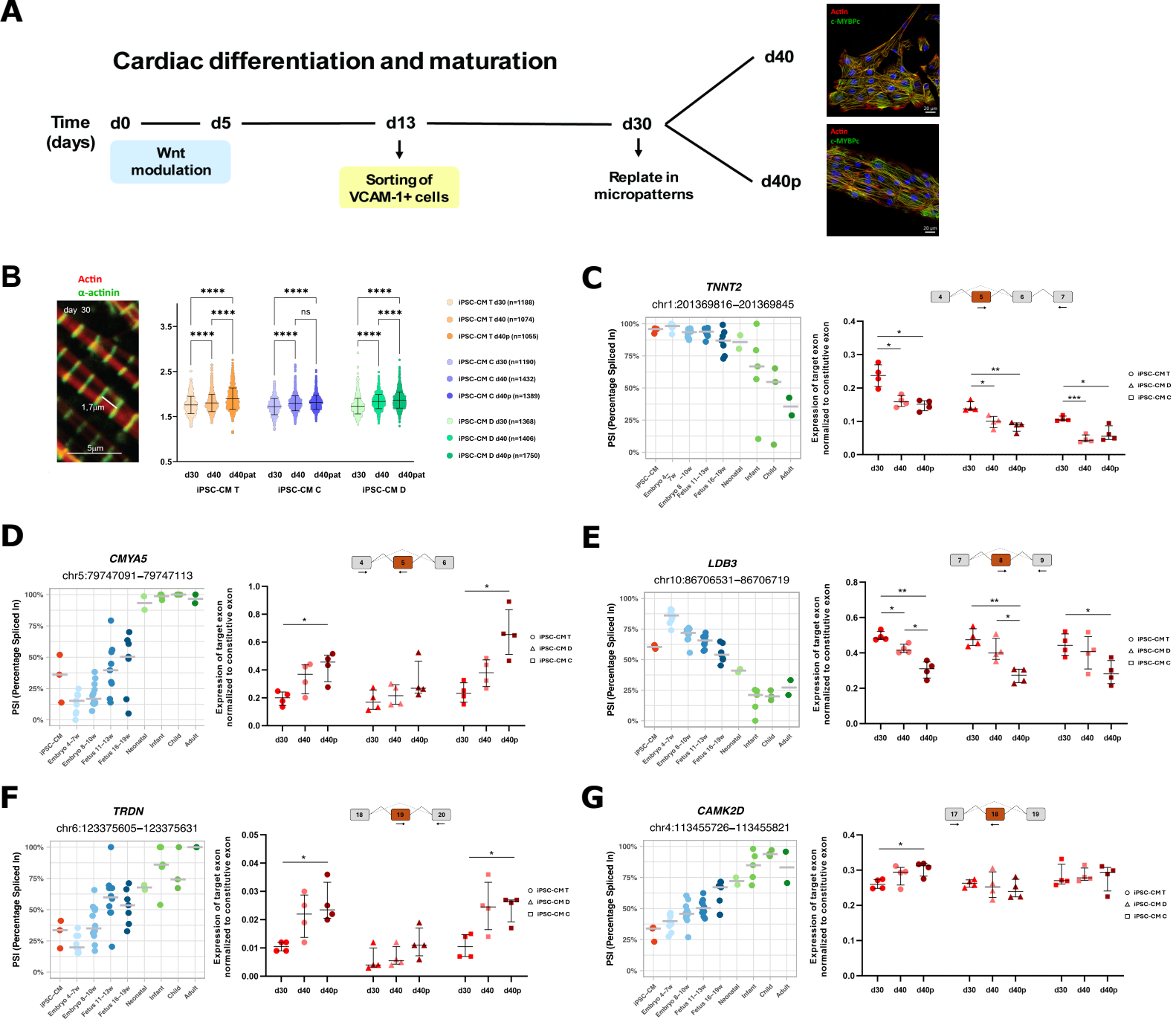
A
Cardiac differentiation and maturation
Time (days)
d0
d5
d13
d30
d40
d40p
Wnt modulation
Sorting of VCAM-1+ cells
Replate in micropatterns
Actin
c-MYBPc
B
Actin
α-actinin
day 30
1,7µm
5µm
iPSC-CM T
iPSC-CM C
iPSC-CM D
d30
d40
d40pat
iPSC-CM T d30 (n=1188)
iPSC-CM T d40 (n=1074)
iPSC-CM T d40p (n=1055)
iPSC-CM C d30 (n=1190)
iPSC-CM C d40 (n=1432)
iPSC-CM C d40p (n=1389)
iPSC-CM D d30 (n=1368)
iPSC-CM D d40 (n=1406)
iPSC-CM D d40p (n=1750)
C
TNNT2
chr1:201369816–201369845
PSI (Percentage Spliced In)
Expression of target exon normalized to constitutive exon
D
CMYA5
chr5:79747091–79747113
E
LDB3
chr10:86706531–86706719
F
TRDN
chr6:123375605–123375631
G
CAMK2D
chr4:113455726–113455821
iPSC-CM
Embryo 4–7w
Embryo 8–10w
Fetus 11–13w
Fetus 16–19w
Neonatal
Infant
Child
Adult